



Shear-flexible subdivision shells

Quan Long, P. Burkhard Bornemann and Fehmi Cirak

Department of Engineering, University of Cambridge, Trumpington Street, Cambridge CB2 1PZ, U.K.

SUMMARY

We present a new shell model and an accompanying discretization scheme that is suitable for thin and thick shells. The deformed configuration of the shell is parameterised using the mid-surface position vector and an additional shear vector for describing the out-of-plane shear deformations. In the limit of vanishing thickness, the shear vector is identically zero and the Kirchhoff-Love model is recovered. Importantly, there are no compatibility constraints to be satisfied by the shape functions used for discretizing the mid-surface and the shear vector. The mid-surface has to be interpolated with smooth C^1 -continuous shape functions, whereas the shear vector can be interpolated with C^0 -continuous shape functions. In the present paper, the mid-surface as well as the shear vector are interpolated with smooth subdivision shape functions. The resulting finite elements are suitable for thin and thick shells and do not exhibit shear locking. The good performance of the proposed formulation is demonstrated with a number of linear and geometrically nonlinear plate and shell examples.

KEY WORDS: shells, subdivision surfaces, isogeometric analysis

1. Introduction

In [11, 10], Cirak et al. used the Kirchhoff-Love shell model in combination with subdivision surfaces for developing particularly robust and efficient thin shell finite elements. The Kirchhoff-Love energy functional depends on the metric and curvature of the shell mid-surface in the reference and deformed configurations. Accordingly, shape functions with square-integrable first and second order derivatives are necessary. In subdivision shells, subdivision surfaces are used for generating the prerequisite smooth shape functions with square integrable second derivatives. Subdivision surfaces originate from computer aided design (see e.g. [34, 22, 21, 9] for an overview) and are, at present, extensively used in computer animation applications [13]. Subdivision surfaces are in general identical to b-splines or NURBS on structured meshes, but they provide provably smooth surfaces on unstructured meshes [23].

As any other shell model, the Kirchhoff-Love model is only an approximation to the inherently three-dimensional deformation state in a thin solid body. It can be mathematically shown that the Kirchhoff-Love model is an asymptotically correct model for a solid in the limit of vanishing thickness [8]. There are many engineering applications involving moderately thick shells for which the Kirchhoff-Love model is insufficient. The accuracy of the Kirchhoff-Love model deteriorates because of the neglected out-of-plane (or, in other terms, transverse) shear energy contribution which becomes important as thickness increases. The Kirchhoff-Love model is also referred to as a shear-rigid model because of the not considered out-of-plane shear deformations. In shear-flexible shell models, like the Reissner-Mindlin model, the energy contribution of the out-of-plane deformations is taken into account, and as a result, such models are better suited for thick shells. Note that the enhanced accuracy comes with an increase in the number of variables so that the Kirchhoff-Love model is still appealing for thin shells.

The parameterisation of the deformations underlying the Reissner-Mindlin model is not unique. The choice of the parameterisation can greatly affect the ease of computational implementation and the conditioning of the resulting discrete equation system. In earlier works on Reissner-Mindlin type shell finite elements typically the displacements

*Correspondence to: f.cirak@eng.cam.ac.uk

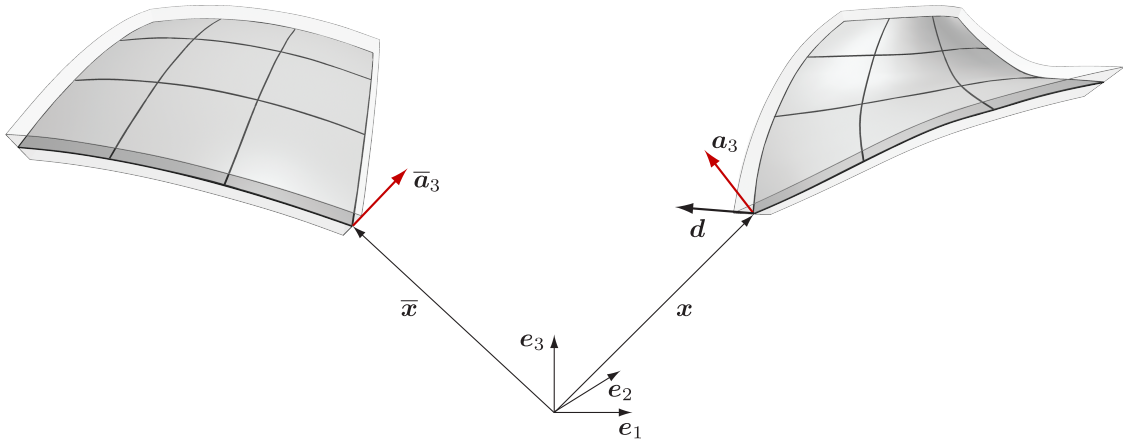


Figure 1. Shell geometry in the reference and the deformed configurations (left and right, respectively).

of the shell mid-surface and the rotations of the shell director are chosen as variables. Although the discretization of finite rotations is not straightforward, it is a well understood and solved problem. Later on, a number of shell models were proposed in which instead of the rotations an additional displacement vector is used for describing the director deformations [26, 7, 3, 5, 25]. In such models the unknown variables are the three components of the mid-surface displacement vector and the three components of the shear vector describing the difference between the deformed and undeformed director. Moreover, in order to facilitate the use of three-dimensional material models, additional variables for describing nonlinear displacements across the thickness are included. All the mentioned Reissner-Mindlin type models lead to energy functionals which contain only the first order derivatives of the displacement variables, which is important for subsequent discussions.

In the present work an alternative parameterisation of the Reissner-Mindlin model is proposed. The variables of the new model are a vector field for describing the shell mid-surface displacements and an additional *shear vector field* for describing the deformation of the director. The standard Kirchhoff-Love model is recovered by setting the shear vector field to zero. Hence, the thin limit is characterised by non-zero mid-surface displacements and a zero shear vector field. In contrast to conventional Reissner-Mindlin type models, the energy functional of the proposed model contains the second order derivatives of the mid-surface displacement field and the first order derivatives of the shear vector field. Therefore, the conforming discretization of the energy functional requires shape functions from the Sobolev space H^2 . In the presented numerical computations, the mid-surface displacement and the shear vector fields are interpolated with subdivision shape functions. Although the subdivision shape functions greatly facilitate the implementation of the proposed model, it would also be possible to use alternative smooth interpolation schemes, such as those presented in [17, 19].

The outline of the paper is as follows. In Section 2 we introduce the proposed shell kinematics and compare it with conventional Kirchhoff-Love and Reissner-Mindlin type models. As a simple comparative example, the bending of a straight beam into a circle is studied. In Section 3 a standard semi-inverse approach is used to derive the energy functional for the proposed model. Shell specific constitutive models and the modifications required to enforce the plane-stress condition are discussed in Section 4. In Section 5, we briefly review subdivision surfaces and then illustrate their use in discretizing the new shell energy functional. Finally, in Section 6 a number of linear and nonlinear plate and shell examples are presented to study the efficiency and robustness of the new shell elements.

2. Shell kinematics

We consider a shell with the mid-surface Ω , thickness \bar{t} and the assumed kinematics

$$\varphi(\theta^1, \theta^2, \theta^3) = x(\theta^1, \theta^2) + \theta^3 d(\theta^1, \theta^2) \quad \text{with } \theta^3 \in [-\bar{t}/2, \bar{t}/2] \quad (1)$$

where φ is the position vector of a material point with the convective (curvilinear) coordinates $(\theta^1, \theta^2, \theta^3)$ and x is the position vector of a material point on the shell mid-surface with the convective coordinates $(\theta^1, \theta^2, \theta^3 \equiv 0)$,

$\bar{\bullet}$	over-bar denotes variables of reference configuration	$\mathbf{g}_i = \frac{\partial \varphi}{\partial \theta^i}$	covariant base vectors
Greek indices	take values 1, 2	$\mathbf{g}^i = \frac{\partial \theta^i}{\partial \varphi}$	contravariant base vectors
Latin indices	take values 1, 2, 3	$g_{ij} = \mathbf{g}_i \cdot \mathbf{g}_j$	components of covariant metric tensor
$\bullet_{,i}$	comma denotes differentiation with respect to θ^i	$g^{ij} = \mathbf{g}^i \cdot \mathbf{g}^j$	components of contravariant metric tensor
$\mathbf{a}_\alpha = \frac{\partial \mathbf{x}}{\partial \theta^\alpha}$	covariant base vectors for $\theta^3 = 0$	$\mathbf{a}_3 = \frac{\mathbf{a}_1 \times \mathbf{a}_2}{ \mathbf{a}_1 \times \mathbf{a}_2 }$	normal to the mid-surface
$\mathbf{a}^\alpha = \frac{\partial \theta^\alpha}{\partial \mathbf{x}}$	contravariant base vectors for $\theta^3 = 0$		

Table I. Notation and definitions.

see Figure 1. The unit vector \mathbf{d} is referred to as the shell director or shell fibre and will be specified below. In order to distinguish the reference and deformed configurations from now on the reference configuration variables will be denoted with an over-bar.

In the reference configuration, the director is chosen to be the mid-surface unit normal so that $\bar{\mathbf{d}} = \bar{\mathbf{a}}_3$ (using the definitions in Table I). In the deformed configuration the director is assumed to be

$$\mathbf{d}(\theta^1, \theta^2) = \frac{\mathbf{a}_1 \times \mathbf{a}_2 + \mathbf{w}}{|\mathbf{a}_1 \times \mathbf{a}_2 + \mathbf{w}|} \quad (2)$$

where \mathbf{w} is a vector added on the non-normalised deformed normal $\mathbf{a}_1 \times \mathbf{a}_2$. Since the purpose of \mathbf{w} is to enable out-of-plane shear deformations, we will refer to it as the *shear vector*.

With the kinematic assumptions (1) and (2) and the definitions of Table I the deformation gradient of the shell can be expressed as

$$\mathbf{F} = \frac{\partial \varphi}{\partial \bar{\varphi}} = \frac{\partial \varphi}{\partial \theta^i} \frac{\partial \theta^i}{\partial \bar{\varphi}} = \mathbf{g}_i \otimes \bar{\mathbf{g}}^i = [\mathbf{a}_\alpha + \theta^3 \mathbf{d}_{,\alpha}] \otimes \bar{\mathbf{g}}^\alpha + \mathbf{d} \otimes \bar{\mathbf{g}}^3 \quad (3)$$

Next, we derive the Green-Lagrange strain tensor of the shell. To this end, first recall the definition of the Green-Lagrange strain tensor for a three-dimensional solid

$$\mathbf{E} = \frac{1}{2} (\mathbf{F}^T \mathbf{F} - \mathbf{I}) = \frac{1}{2} (g_{ij} - \bar{g}_{ij}) \bar{\mathbf{g}}^i \otimes \bar{\mathbf{g}}^j \quad (4)$$

Then, considering the kinematic assumptions we obtain

$$\mathbf{E} = \boldsymbol{\alpha} + \theta^3 \boldsymbol{\beta} + (\theta^3)^2 \dots \quad (5)$$

with the components

$$\alpha_{\alpha\beta} = \frac{1}{2} (\mathbf{a}_\alpha \cdot \mathbf{a}_\beta - \bar{\mathbf{a}}_\alpha \cdot \bar{\mathbf{a}}_\beta) \quad (6a)$$

$$\alpha_{\alpha 3} = \alpha_{3\alpha} = \frac{1}{2} \mathbf{a}_\alpha \cdot \mathbf{d} \quad (6b)$$

$$\alpha_{33} = 0 \quad (6c)$$

$$\beta_{\alpha\beta} = \frac{1}{2} (\mathbf{a}_\alpha \cdot \mathbf{d}_{,\beta} + \mathbf{a}_\beta \cdot \mathbf{d}_{,\alpha} - \bar{\mathbf{a}}_\alpha \cdot \bar{\mathbf{a}}_{3,\beta} - \bar{\mathbf{a}}_\beta \cdot \bar{\mathbf{a}}_{3,\alpha}) \quad (6d)$$

$$\beta_{\alpha 3} = \beta_{3\alpha} = \beta_{33} = 0 \quad (6e)$$

where we used the relations $\bar{\mathbf{a}}_\alpha \cdot \bar{\mathbf{a}}_3 = 0$ and $\mathbf{d}_{,\alpha} \cdot \mathbf{d} = 0$. In (5) the quadratic terms have been neglected as it is common in most shell theories.

To gain physical insight into the strain expressions (6) it is helpful to recall that $\mathbf{a}_\alpha \cdot \mathbf{a}_\beta$ is the first and $\mathbf{a}_\alpha \cdot \mathbf{a}_{3,\beta}$ is the second fundamental form of the shell mid-surface. Hence, the components $\alpha_{\alpha\beta}$ measure the straining of the mid-surface and the components $\beta_{\alpha\beta}$ measure the change in curvature when $\mathbf{w} = \mathbf{0}$. Furthermore, the strain components $\alpha_{\alpha 3}$ measure the out-of-plane shearing and are zero when $\mathbf{w} = \mathbf{0}$.

2.1. Illustrative comparison of the proposed kinematics with conventional models

In order to provide an illustrative comparison of the various kinematic models, we consider a beam embedded in the two-dimensional $(\mathbf{e}_1, \mathbf{e}_3)$ -plane. The difference between the various beam models concerns the assumed deformation of the beam cross-section.

2.1.1. Euler-Bernoulli model In the Euler-Bernoulli theory, which corresponds to the Kirchhoff-Love theory for shells, the deformed configuration is assumed to be

$$\varphi(\theta^1, \theta^2, \theta^3) = \mathbf{x}(\theta^1) + \theta^2 \mathbf{e}_2 + \theta^3 \mathbf{a}_3(\theta^1) \quad (7)$$

where $\mathbf{x}(\theta^1) = x^1(\theta^1)\mathbf{e}_1 + x^3(\theta^1)\mathbf{e}_3$ is the deformed axis of the beam, \mathbf{e}_2 is the direction orthogonal to the $(\mathbf{e}_1, \mathbf{e}_3)$ -plane, $\mathbf{a}_3(\theta^1)$ is the normal to the deformed beam axis and θ^1 is a path parameter along the beam axis. The normal \mathbf{a}_3 is given by

$$\mathbf{a}_3(\theta^1) = \frac{\mathbf{x}(\theta^1)_{,1} \times \mathbf{e}_2}{|\mathbf{x}(\theta^1)_{,1} \times \mathbf{e}_2|} \quad (8)$$

Thus, the deformed configuration depends only on the deformed position vector of the beam axis \mathbf{x}

$$\varphi(\theta^1, \theta^2, \theta^3) = \mathbf{x}(\theta^1) + \theta^2 \mathbf{e}_2 + \theta^3 \frac{\mathbf{x}(\theta^1)_{,1} \times \mathbf{e}_2}{|\mathbf{x}(\theta^1)_{,1} \times \mathbf{e}_2|} \quad (9)$$

2.1.2. Timoshenko model In the Timoshenko theory, which corresponds to the Reissner-Mindlin theory for shells, the deformed configuration is assumed to be

$$\varphi(\theta^1, \theta^2, \theta^3) = \mathbf{x}(\theta^1) + \theta^2 \mathbf{e}_2 + \theta^3 \mathbf{d}(\theta^1) \quad (10)$$

In contrast to the Euler-Bernoulli model, the unit-length director \mathbf{d} allows transverse shear strains to occur. The director deformations can be parameterised with a rotation matrix $\mathbf{R}(\chi)$ which depends on a rotation angle $\chi(\theta^1)$

$$\mathbf{d} = \mathbf{R}(\chi) \bar{\mathbf{a}}_3 \quad (11)$$

Consequently, the deformed configuration depends on the deformed beam axis $\mathbf{x}(\theta^1)$ and the rotation angle $\chi(\theta^1)$, i.e.

$$\varphi(\theta^1, \theta^2, \theta^3) = \mathbf{x}(\theta^1) + \theta^2 \mathbf{e}_2 + \theta^3 \mathbf{R}(\chi) \bar{\mathbf{a}}_3 \quad (12)$$

2.1.3. Proposed model In the new kinematics introduced in Section 2, the deformed configuration is assumed to be

$$\varphi(\theta^1, \theta^2, \theta^3) = \mathbf{x}(\theta^1) + \theta^2 \mathbf{e}_2 + \theta^3 \frac{\mathbf{a}_1 \times \mathbf{a}_2 + \mathbf{w}}{|\mathbf{a}_1 \times \mathbf{a}_2 + \mathbf{w}|} \quad (13)$$

The deformed configuration depends on the deformed position vector of the beam axis $\mathbf{x}(\theta^1)$ and the shear vector $\mathbf{w}(\theta^1)$. This becomes more apparent after expressing the tangent vector $\mathbf{a}_1(\theta^1)$ in terms of the beam axis

$$\varphi(\theta^1, \theta^2, \theta^3) = \mathbf{x}(\theta^1) + \theta^2 \mathbf{e}_2 + \theta^3 \frac{\mathbf{x}(\theta^1)_{,1} \times \mathbf{e}_2 + \mathbf{w}(\theta^1)}{|\mathbf{x}(\theta^1)_{,1} \times \mathbf{e}_2 + \mathbf{w}(\theta^1)|} \quad (14)$$

Since the shear vector \mathbf{w} is unconstrained, transverse shear strains are possible.

2.1.4. *Example: Beam deformation with constant curvature* We consider an initially straight cantilever beam whose reference configuration is described with

$$\bar{\varphi}(\theta^1, \theta^2, \theta^3) = \underbrace{\begin{pmatrix} \theta^1 \\ 0 \\ 0 \end{pmatrix}}_{\bar{\mathbf{x}}} + \theta_2 \underbrace{\begin{pmatrix} 0 \\ 1 \\ 0 \end{pmatrix}}_{\mathbf{e}_2} + \theta^3 \underbrace{\begin{pmatrix} 0 \\ 0 \\ 1 \end{pmatrix}}_{\bar{\mathbf{d}} = \bar{\mathbf{a}}_3} \quad (15)$$

The beam is deformed into a circular arc with radius R without changing the length of the beam axis and without applying transverse shear deformations so that the deformed configuration is

$$\varphi(\theta^1, \theta^2, \theta^3) = \underbrace{\begin{pmatrix} R \sin \frac{\theta^1}{R} \\ 0 \\ R - R \cos \frac{\theta^1}{R} \end{pmatrix}}_{\mathbf{x}(\theta^1)} + \theta_2 \underbrace{\begin{pmatrix} 0 \\ 1 \\ 0 \end{pmatrix}}_{\mathbf{e}_2} + \theta^3 \underbrace{\begin{pmatrix} -\sin \frac{\theta^1}{R} \\ 0 \\ \cos \frac{\theta^1}{R} \end{pmatrix}}_{\mathbf{d}(\theta^1)} \quad (16)$$

In the following the out-of-plane shear deformation of the beam according to the different beam models is computed. To begin with we determine the out-of-plane shear deformation component of the Green-Lagrange strain tensor as defined for the solid

$$\begin{aligned} E_{13} &= \frac{1}{2} (g_{13} - \bar{g}_{13}) = \frac{1}{2} (\varphi_{,1} \cdot \varphi_{,3} - \bar{\varphi}_{,1} \cdot \bar{\varphi}_{,3}) \\ &= \frac{1}{2} \left[\begin{pmatrix} \cos \frac{\theta^1}{R} \\ 0 \\ \sin \frac{\theta^1}{R} \end{pmatrix} + \theta_3 \begin{pmatrix} -\frac{1}{R} \cos \frac{\theta^1}{R} \\ 0 \\ -\frac{1}{R} \sin \frac{\theta^1}{R} \end{pmatrix} \right] \cdot \begin{pmatrix} -\sin \frac{\theta^1}{R} \\ 0 \\ \cos \frac{\theta^1}{R} \end{pmatrix} = 0 \end{aligned} \quad (17)$$

This result is not surprising considering that the director is equal to the unit normal of the deformed beam axis, i.e. $\mathbf{d} = \mathbf{a}_3$. Moreover, the given deformed configuration can be exactly represented with the Bernoulli model in which the director is assumed to be normal to the deformed beam axis.

For the Timoshenko model, the director is obtained by rotating the normal to the reference beam axis, i.e. $\mathbf{d} = \mathbf{R}(\chi)\bar{\mathbf{a}}_3$. The degrees of freedom are the deformed beam axis \mathbf{x} and the rotation angle χ . For the considered deformed beam, the out-of-plane shear deformation according to the Timoshenko model is

$$E_{13} = \frac{1}{2} \left[\begin{pmatrix} \cos \frac{\theta^1}{R} \\ 0 \\ \sin \frac{\theta^1}{R} \end{pmatrix} + \theta_3 \mathbf{R}(\chi)_{,1} \begin{pmatrix} 0 \\ 0 \\ 1 \end{pmatrix} \right] \cdot \left[\mathbf{R}(\chi) \begin{pmatrix} 0 \\ 0 \\ 1 \end{pmatrix} \right] = \frac{1}{2} \begin{pmatrix} \cos \frac{\theta^1}{R} \\ 0 \\ \sin \frac{\theta^1}{R} \end{pmatrix} \cdot \begin{pmatrix} -\sin \chi \\ 0 \\ \cos \chi \end{pmatrix} \quad (18)$$

By choosing $\chi = \theta^1/R$ the zero out-of-plane shear deformation of the solid model can be reproduced. In a finite element discretized Timoshenko model the unknowns are the deformed beam axis \mathbf{x} and the rotation angle χ . In order to reproduce the zero out-of-plane shear deformations the finite element function spaces for \mathbf{x} and χ have to be carefully chosen so that the discretized version of (18) yields zero.

In the proposed kinematic model the degrees of freedom are the deformed beam axis \mathbf{x} and the shear vector \mathbf{w} . The deformed configuration is reproduced if the shear vector \mathbf{w} is set to zero, cf. (14) and (16). In other words, the proposed kinematics exactly reduces to the Euler-Bernoulli model if no shear deformations are present. As a consequence, in a finite element context, there is no need to match the finite element function spaces used for discretizing the deformed beam axis \mathbf{x} and the shear vector \mathbf{w} .

3. Weak form of equilibrium equations

We consider the potential energy of a hyperelastic shell for deriving the shell equilibrium equations in the weak form

$$\Pi(\varphi) = \Pi_{\text{int}}(\varphi) + \Pi_{\text{ext}}(\varphi) \quad (19)$$

where Π_{int} is the internal and Π_{ext} is the external potential energy. At equilibrium configurations the first variation of the potential energy is zero

$$\delta\Pi = \delta\Pi_{\text{int}} + \delta\Pi_{\text{ext}} = 0 \quad (20)$$

The internal potential energy is the integral of the strain energy density $W(\mathbf{E})$ which is a function of the Green-Lagrange strain tensor \mathbf{E}

$$\Pi_{\text{int}}(\varphi) = \int_{\bar{\Omega}} \int_{-\frac{\bar{t}}{2}}^{\frac{\bar{t}}{2}} W(\mathbf{E}(\varphi)) \bar{j} \, d\theta^3 \, d\bar{\Omega} \quad (21)$$

Here, the Jacobian \bar{j} takes into account the curvature of the shell in the integration across the thickness

$$\bar{j} = \frac{|(\bar{\mathbf{g}}_1 \times \bar{\mathbf{g}}_2) \cdot \bar{\mathbf{g}}_3|}{|(\bar{\mathbf{a}}_1 \times \bar{\mathbf{a}}_2) \cdot \bar{\mathbf{a}}_3|} \quad (22)$$

The variation of the internal energy reads

$$\delta\Pi_{\text{int}} = \int_{\bar{\Omega}} \int_{-\frac{\bar{t}}{2}}^{\frac{\bar{t}}{2}} \frac{\partial W(\mathbf{E})}{\partial \mathbf{E}} : \delta \mathbf{E} \bar{j} \, d\theta^3 \, d\bar{\Omega} = \int_{\bar{\Omega}} \int_{-\frac{\bar{t}}{2}}^{\frac{\bar{t}}{2}} \mathbf{S} : \delta \mathbf{E} \bar{j} \, d\theta^3 \, d\bar{\Omega} \quad (23)$$

where \mathbf{S} is the second Piola-Kirchhoff stress tensor. After introducing the Green-Lagrange strain (5), the preceding equation becomes

$$\delta\Pi_{\text{int}} = \int_{\bar{\Omega}} \int_{-\frac{\bar{t}}{2}}^{\frac{\bar{t}}{2}} \mathbf{S} : (\delta \boldsymbol{\alpha} + \theta^3 \delta \boldsymbol{\beta}) \bar{j} \, d\theta^3 \, d\bar{\Omega} \quad (24)$$

Next, the membrane stress and moment resultants are defined

$$\mathbf{n} = \int_{-\frac{\bar{t}}{2}}^{\frac{\bar{t}}{2}} \mathbf{S} \bar{j} \, d\theta^3 \quad (25a)$$

$$\mathbf{m} = \int_{-\frac{\bar{t}}{2}}^{\frac{\bar{t}}{2}} \theta^3 \mathbf{S} \bar{j} \, d\theta^3 \quad (25b)$$

which enable us to write the variation of the internal energy as an integral over the shell mid-surface

$$\delta\Pi_{\text{int}} = \int_{\bar{\Omega}} (\mathbf{n} : \delta \boldsymbol{\alpha} + \mathbf{m} : \delta \boldsymbol{\beta}) \, d\bar{\Omega} \quad (26)$$

Recall that the independent variables in the new model are the mid-surface position \mathbf{x} and the shear vector \mathbf{w} . The variation of the internal energy with respect to the two independent variables is

$$\delta\Pi_{\text{int}} = \int_{\bar{\Omega}} \left[\left(\mathbf{n} : \frac{\partial \boldsymbol{\alpha}}{\partial \mathbf{x}} + \mathbf{m} : \frac{\partial \boldsymbol{\beta}}{\partial \mathbf{x}} \right) \cdot \delta \mathbf{x} + \left(\mathbf{n} : \frac{\partial \boldsymbol{\alpha}}{\partial \mathbf{w}} + \mathbf{m} : \frac{\partial \boldsymbol{\beta}}{\partial \mathbf{w}} \right) \cdot \delta \mathbf{w} \right] \, d\bar{\Omega} \quad (27)$$

Next we derive the variation of the external potential energy of the shell. The boundary of the shell consists of the top, bottom and lateral surfaces of which, for brevity, only the lateral surface $[-\bar{h}/2, \bar{h}/2] \times \bar{\Gamma}$ will be considered. The external potential energy of the shell with the external body force vector \mathbf{b} and the external lateral surface traction vector \mathbf{f} is given by

$$\Pi_{\text{ext}}(\varphi) = - \int_{\bar{\Omega}} \int_{-\frac{\bar{t}}{2}}^{\frac{\bar{t}}{2}} \mathbf{b} \cdot (\mathbf{x} + \theta^3 \mathbf{d}) \bar{j} \, d\theta^3 \, d\bar{\Omega} - \int_{\bar{\Gamma}} \int_{-\frac{\bar{t}}{2}}^{\frac{\bar{t}}{2}} \mathbf{f} \cdot (\mathbf{x} + \theta^3 \mathbf{d}) \bar{j} \, d\theta^3 \, d\bar{\Gamma} \quad (28)$$

whereby the kinematic assumption (1) has been used. Furthermore, we define the following external force and moment resultants

$$\mathbf{p} = \int_{-\frac{\bar{t}}{2}}^{\frac{\bar{t}}{2}} \mathbf{b} \bar{j} \, d\theta^3 \quad \mathbf{q} = \int_{-\frac{\bar{t}}{2}}^{\frac{\bar{t}}{2}} \theta^3 \mathbf{b} \bar{j} \, d\theta^3 \quad (29a)$$

$$\mathbf{r} = \int_{-\frac{\bar{t}}{2}}^{\frac{\bar{t}}{2}} \mathbf{f} \bar{j} \, d\theta^3 \quad \mathbf{s} = \int_{-\frac{\bar{t}}{2}}^{\frac{\bar{t}}{2}} \theta^3 \mathbf{f} \bar{j} \, d\theta^3 \quad (29b)$$

Thus, the variation of the external energy with respect to the mid-surface position \mathbf{x} and shear vector \mathbf{w} can be expressed as

$$\delta\Pi_{\text{ext}} = - \int_{\bar{\Omega}} \left[\left(\mathbf{p} + \mathbf{q} \frac{\partial \mathbf{d}}{\partial \mathbf{x}} \right) \cdot \delta \mathbf{x} + \mathbf{q} \frac{\partial \mathbf{d}}{\partial \mathbf{w}} \cdot \delta \mathbf{w} \right] d\bar{\Omega} - \int_{\bar{\Gamma}} \left[\left(\mathbf{r} + \mathbf{s} \frac{\partial \mathbf{d}}{\partial \mathbf{x}} \right) \cdot \delta \mathbf{x} + \mathbf{s} \frac{\partial \mathbf{d}}{\partial \mathbf{w}} \cdot \delta \mathbf{w} \right] d\bar{\Gamma} \quad (30)$$

Combining the variations of the internal and external energy yields the weak form of the shell equilibrium equations

$$\left(\frac{\partial \Pi_{\text{int}}(\mathbf{x}, \mathbf{w})}{\partial \mathbf{x}} + \frac{\partial \Pi_{\text{ext}}(\mathbf{x}, \mathbf{w})}{\partial \mathbf{x}} \right) \cdot \delta \mathbf{x} = \mathbf{0} \quad (31a)$$

$$\left(\frac{\partial \Pi_{\text{int}}(\mathbf{x}, \mathbf{w})}{\partial \mathbf{w}} + \frac{\partial \Pi_{\text{ext}}(\mathbf{x}, \mathbf{w})}{\partial \mathbf{w}} \right) \cdot \delta \mathbf{w} = \mathbf{0} \quad (31b)$$

Finally, a comment is warranted concerning the Dirichlet boundary conditions. From the expression for the external potential energy (28) and definitions (29a) and (29b) it can be deduced that the variable conjugate to the external moments is the director \mathbf{d} . This implies that for enforcing rotation boundary conditions the vector $\mathbf{a}_1 \times \mathbf{a}_2 + \mathbf{w}$ has to be constrained to the prescribed value.

4. Constitutive equations

In this section we briefly summarise the linear elastic material model used. For the proposed shell model it is crucial that the constitutive equations satisfy the plane stress condition, i.e. have zero through-the-thickness stress. Moreover, the amount of shear must remain within the limits of Reissner-Mindlin model. As discussed in previous works, e.g., [7, 24], three-dimensional constitutive models may only be used if the kinematic assumptions include higher than linear displacements across the thickness.

The internal energy density of a linear elastic isotropic material under plane stress conditions is given by

$$W(\mathbf{E}) = \frac{1}{2} \mathbf{E} : \mathbf{C} : \mathbf{E} \quad (32)$$

where \mathbf{C} is a fourth order constitutive tensor

$$\mathbf{C} = C^{ijkl} \bar{\mathbf{g}}_i \otimes \bar{\mathbf{g}}_j \otimes \bar{\mathbf{g}}_k \otimes \bar{\mathbf{g}}_l \quad (33)$$

with components

$$C^{\alpha\beta\lambda\mu} = \frac{E}{2(1+\nu)} \left(\bar{g}^{\alpha\lambda} \bar{g}^{\beta\mu} + \bar{g}^{\alpha\mu} \bar{g}^{\beta\lambda} + \frac{2\nu}{1-\nu} \bar{g}^{\alpha\beta} \bar{g}^{\lambda\mu} \right) \quad (34a)$$

$$C^{\alpha 3 \lambda 3} = \frac{E}{2(1+\nu)} \bar{g}^{\alpha\lambda} \quad (34b)$$

$$C^{3333} = C^{\alpha\beta 33} = 0 \quad (34c)$$

and Young's modulus E and Poisson's ratio ν .

The shell internal energy density in stress resultant form is obtained by introducing the constitutive tensor components (34) and the shell kinematics (6) into (32) and then integrating across the thickness

$$\begin{aligned} W(\boldsymbol{\alpha}, \boldsymbol{\beta}) &= \frac{1}{2} \frac{E\bar{t}}{1-\nu^2} H^{\alpha\beta\gamma\delta} \alpha_{\alpha\beta} \alpha_{\gamma\delta} + \frac{1}{2} \frac{E\bar{t}^3}{12(1-\nu^2)} H^{\alpha\beta\gamma\delta} \beta_{\alpha\beta} \beta_{\gamma\delta} \\ &+ \frac{1}{2} \frac{\kappa E\bar{t}}{1+\nu} \bar{a}^{\alpha\beta} \alpha_{\alpha 3} \alpha_{\beta 3} + \frac{1}{2} \frac{\kappa E\bar{t}^3}{12(1+\nu)} \bar{a}^{\alpha\beta} \beta_{\alpha 3} \beta_{\beta 3} \end{aligned} \quad (35)$$

with

$$H^{\alpha\beta\gamma\delta} = \frac{1-\nu}{2} (\bar{a}^{\alpha\gamma} \bar{a}^{\beta\delta} + \bar{a}^{\alpha\delta} \bar{a}^{\beta\gamma}) + \nu \bar{a}^{\alpha\beta} \bar{a}^{\gamma\delta}$$

The shear correction factor $\kappa = 5/6$ takes into account that the actual out-of-plane shear strains are not linear and vanish on top and bottom shell surfaces. Furthermore, note that the derivation of internal energy density in stress

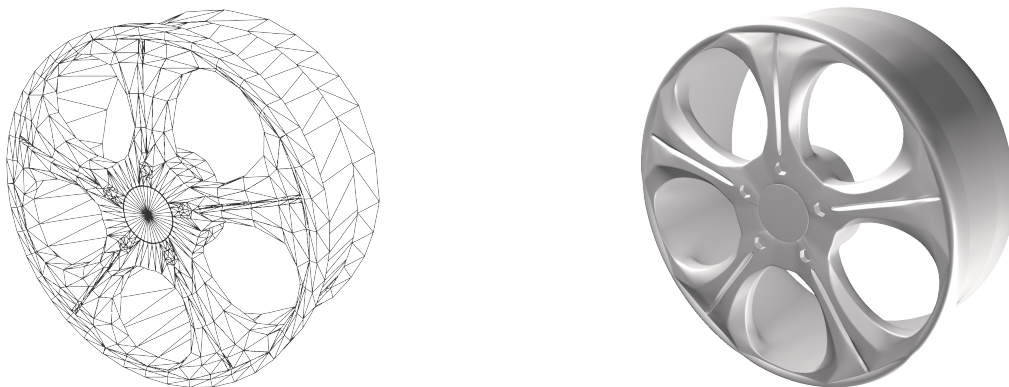


Figure 2. Control mesh of a car wheel rim (left) and the corresponding limit surface obtained with the Loop's subdivision scheme (right).

resultant form (35) contains certain geometric assumptions, such as $\bar{g}^{ij} \approx \bar{a}^{ij}$, see e.g. [18] for details. In case of nonlinear materials it is generally not possible to derive a closed form expression for the internal energy density under plane stress conditions. However, the plane stress assumption can be iteratively pointwise enforced by requiring

$$S^{33} = \frac{\partial W(\mathbf{E})}{\partial E_{33}} = 0 \quad (36)$$

see [10] for details.

5. Discretization of the shell weak form

In contrast to conventional shear-deformable shell models the proposed kinematics contains the second order derivatives of the deformed mid-surface. Hence smooth, or more formally H^2 -conforming, shape functions are necessary for a conforming finite element discretization. In this work, we use the subdivision surfaces, or more precisely, the corresponding subdivision shape functions, for the discretization of the shell weak form. This is in line with our previous work on the discretization of Kirchhoff-Love thin shells with subdivision surfaces [11, 10, 9].

5.1. Brief review of subdivision surfaces

As known splines are only defined on tensor product meshes or, more generally, on meshes with shift-invariant connectivity. This imposes limitations on the type of meshes that can be used and type of objects that can be represented with splines. Subdivision is a generic technique for generalising splines to meshes with arbitrary connectivity [34, 32, 21, 9]. On mesh patches with tensor product or shift-invariant connectivity, subdivision uses the refinability, or in other words the two-scale relation, of b-splines to generate smooth surfaces by successive refinement and averaging. The refinability property of b-splines makes it possible to represent a coarse mesh shape function as a linear combination of shape functions on a finer mesh.

In this work we use Loop's subdivision scheme [16] which is the generalisation of quartic box-splines to arbitrary connectivity meshes. Quartic box-splines are defined on shift-invariant three-direction meshes, which in this context means that the mesh consists only of triangles and that each vertex is connected by six triangles. In contrast to quartic box-splines, in Loop's scheme the number of triangles connected to a vertex can be arbitrary and the resulting surface is at least C^1 -continuous. In line with other subdivision schemes, Loop's scheme decomposes each subdivision step into a refinement and an averaging step. In the refinement step the mesh is refined by quadrisecting the triangles. Subsequently, the coordinates of each vertex are recomputed as a weighted average of the vertex coordinates of the neighbouring vertices. In the subdivision literature, the averaging weights are usually given in form of *subdivision masks* as shown in Figure 3. The vertex mask is used for recomputing the coordinates of vertices which have already existed on the coarse mesh. The edge mask is used for computing the coordinates of vertices introduced on the edges during the quadrisecting. Note that the averaging weights depend only on the connectivity of the mesh and not on the actual vertex coordinates.

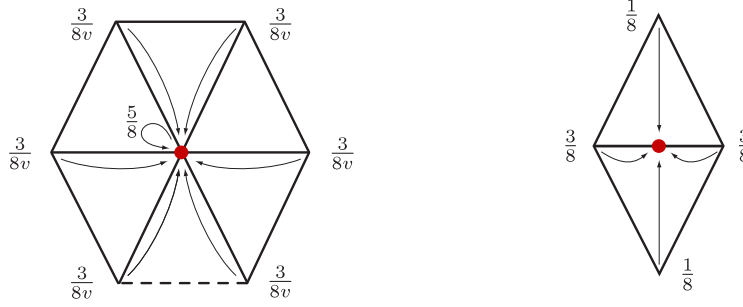


Figure 3. Vertex and edge masks for standard vertices and edges (i.e., non-boundary and non-corner). The number of triangles attached to the vertex is the valence v of the vertex. The dashed edge emphasises that the vertex mask applies to vertices with arbitrary valence.

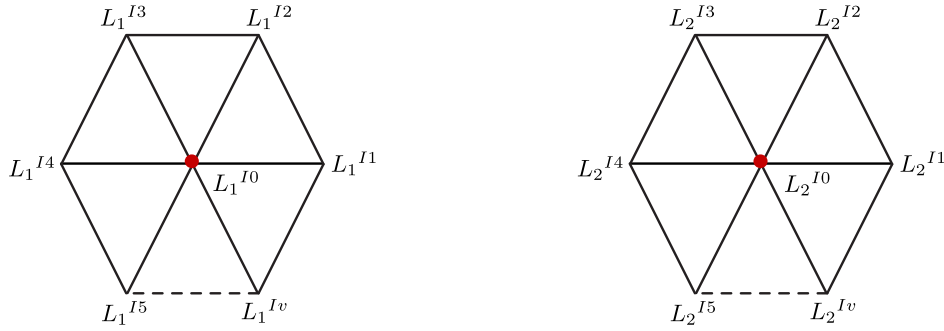


Figure 4. Masks for computing the two tangent vectors to the limit surface.

The convergence and smoothness properties of subdivision surfaces can also be established without referring to their spline origin, see [9] for details and references. To this end, subdivision is considered as a linear mapping from a coarse to a fine mesh. Under some technical conditions, the eigenstructure of the mapping yields masks for computing the limit position and the tangent plane to the limit surface at the vertices. For example, the two masks shown in Figure 4 for computing the two tangent vectors \mathbf{t}_1^I and \mathbf{t}_2^I have been determined from the eigenvectors of the subdivision mapping

$$\mathbf{t}_1^I = \sum_{J=0}^v L_1^{IJ} \mathbf{x}_{J(I)} \quad \mathbf{t}_2^I = \sum_{J=0}^v L_2^{IJ} \mathbf{x}_{J(I)} \quad (37)$$

with

$$\begin{aligned} L_1^{I0} &= 0 & L_1^{IJ} &= \cos\left(\frac{2\pi(J-1)}{v}\right) \\ L_2^{I0} &= 0 & L_2^{IJ} &= \sin\left(\frac{2\pi(J-1)}{v}\right) \end{aligned}$$

where $\mathbf{x}_{J(I)}$ are the vertex coordinates of the finite element mesh in the neighbourhood of node I . The two vectors \mathbf{t}_1^I and \mathbf{t}_2^I are the tangents to the limit surface and not to the triangular mesh. In the following, the two tangent vectors will be used for computing the shell normal at the vertices. It is worth emphasising that by using the limit masks only the surface and its tangents at vertices can be computed.

Subdivision surfaces are parameterised in order to compute quantities, such as the limit position and curvature, at arbitrary locations, like at quadrature points. As previously pointed out, Loop's subdivision leads to box-splines on patches containing only regular vertices. Furthermore, using the well-known correspondence between the box-spline and Bezier shape functions, on regular patches Bezier shape functions can be used for parameterisation. In practical terms, on a regular patch, such as shown in Figure 5, the surface within the centre element is interpolated with

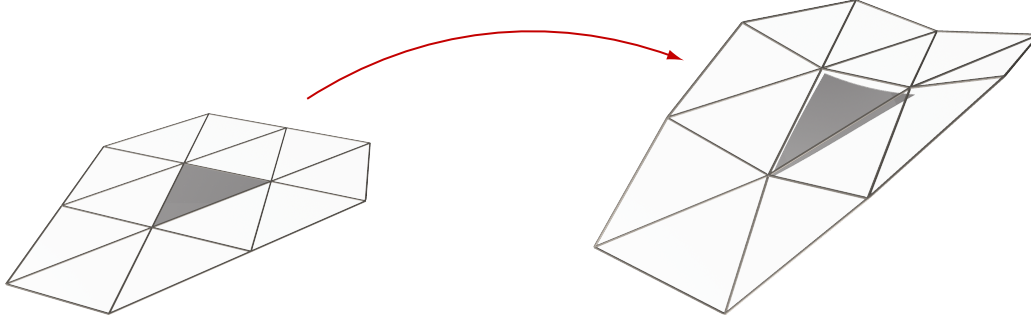


Figure 5. Control patch of a triangular element in the parameter space (left) and in the physical space (right). In the shaded element only the shape functions associated to the shown vertices are non-zero.

$$\mathbf{x}(\theta^1, \theta^2) = \sum_{I=0}^{11} N^I(\theta^1, \theta^2) \mathbf{x}_I \quad (38)$$

where N^I are the twelve Bezier shape functions and \mathbf{x}_I are the coordinates of the corresponding vertices. As shown in [28], irregular patches can be parameterised using Bezier shape functions after sufficient number of subdivisions. For the purpose of this paper, it is sufficient to know that such a parameterisation is available. For details we refer to [11, 9].

5.2. Discretized shell weak form

In the assumed shell kinematics (2), the rotation of the director with respect to the deformed mid-surface normal is parameterised using the shear vector. Moreover, since the length of the director is by definition constrained to unity, the shear vector can only be a vector with two unknown components. In this section, two alternative discretization approaches are introduced which differ only in the consideration of the shear vector. In the first approach, the shear vector has at each finite element node three independent components but an additional director length constraint per node is introduced. The nodal constraint is enforced using Lagrange multipliers so that each node has in total seven degrees of freedom. In the second approach, the shear vector is expressed in the local curvilinear convective frame at each node and has only the two in-plane components as unknowns. This leads to a discretization scheme with only five degrees of freedom per node.

In both approaches subdivision shape functions are used for interpolating the reference and deformed shell mid-surface and the shear vector. The interpolation equations within each triangular element are given by

$$\bar{\mathbf{x}}(\theta^1, \theta^2) = \sum_{I=0}^{NSP-1} N^I(\theta^1, \theta^2) \bar{\mathbf{x}}_I \quad (39a)$$

$$\mathbf{x}(\theta^1, \theta^2) = \sum_{I=0}^{NSP-1} N^I(\theta^1, \theta^2) \mathbf{x}_I \quad (39b)$$

$$\mathbf{w}(\theta^1, \theta^2) = \sum_{I=0}^{NSP-1} N^I(\theta^1, \theta^2) \mathbf{w}_I \quad (39c)$$

where NSP is the number of vertices in the one-neighbourhood of the triangular element and N^I are the subdivision shape functions. Closed form expressions for shape functions are only available on regular patches. For irregular patches we have only an algorithm for evaluating the shape functions and their derivatives at arbitrary locations (θ^1, θ^2) , see [11, 9] for details.

As in conventional finite elements, the partition of unity property of subdivision shape functions allows to write the shell weak form (20) as the sum of NEL element contributions. In addition, introducing the interpolation equations

(39) into the weak form (31) leads to a set of discrete equilibrium equations

$$\begin{pmatrix} \hat{\mathbf{f}}^I(\mathbf{x}_L, \mathbf{w}_L) \\ \tilde{\mathbf{f}}^I(\mathbf{x}_L, \mathbf{w}_L) \end{pmatrix} = \begin{pmatrix} \sum_{K=0}^{NEL-1} \frac{\partial \Pi_{\text{int}}^K}{\partial \mathbf{x}_I} + \sum_{K=0}^{NEL-1} \frac{\partial \Pi_{\text{ext}}^K}{\partial \mathbf{x}_I} \\ \sum_{K=0}^{NEL-1} \frac{\partial \Pi_{\text{int}}^K}{\partial \mathbf{w}_I} + \sum_{K=0}^{NEL-1} \frac{\partial \Pi_{\text{ext}}^K}{\partial \mathbf{w}_I} \end{pmatrix} = \mathbf{0} \quad (40)$$

where the first and second rows represent the local force vectors at node I corresponding to its nodal position and shear vector, respectively. To be precise, the foregoing summations imply the presence of a mapping between the global (i.e., mesh-wide) and local (i.e., element specific) vertex numbering. As an example, the internal force contribution of an element K to a vertex I is computed with

$$\hat{\mathbf{f}}_{\text{int}}^{IK}(\mathbf{x}_L, \mathbf{w}_L) = \int_{\bar{\Omega}_K} \left(\mathbf{n} : \frac{\partial \boldsymbol{\alpha}}{\partial \mathbf{x}_I} + \mathbf{m} : \frac{\partial \boldsymbol{\beta}}{\partial \mathbf{x}_I} \right) d\bar{\Omega} \quad (41a)$$

$$\tilde{\mathbf{f}}_{\text{int}}^{IK}(\mathbf{x}_L, \mathbf{w}_L) = \int_{\bar{\Omega}_K} \left(\mathbf{n} : \frac{\partial \boldsymbol{\alpha}}{\partial \mathbf{w}_I} + \mathbf{m} : \frac{\partial \boldsymbol{\beta}}{\partial \mathbf{w}_I} \right) d\bar{\Omega} \quad (41b)$$

5.2.1. Lagrange multiplier constrained shear vector The shear vector can be expressed in the global Cartesian coordinate system so that it has three unknown components at each finite element node

$$\mathbf{w}_I = w^1_I \mathbf{e}_1 + w^2_I \mathbf{e}_2 + w^3_I \mathbf{e}_3 \quad (42)$$

If the shear vector in the interpolation equation (39c) and discrete equilibrium equations (40) is interpreted in the sense of (42), the resulting system of equations is rank deficient. This is due to the used plane stress constitutive model, which does not lead to an equilibrium equation across the shell thickness. Therefore, as mentioned above, an additional constraint equation is introduced in order to constrain the nodal shear vector to the tangential plane of the mid-surface by enforcing

$$[\mathbf{t}_1^I \times \mathbf{t}_2^I] \cdot \mathbf{w}_I = 0 \quad (43)$$

where the two tangent vectors \mathbf{t}_1^I and \mathbf{t}_2^I at node I are computed with the masks given in Section 5.1. In the present work, the Lagrange multiplier method is used to enforce the constraint equation. The equilibrium equations at vertex I are augmented as follows

$$\begin{pmatrix} \hat{\mathbf{f}}^I(\mathbf{x}_L, \mathbf{w}_L, \lambda_L) \\ \tilde{\mathbf{f}}^I(\mathbf{x}_L, \mathbf{w}_L, \lambda_L) \\ 0 \end{pmatrix} = \begin{pmatrix} \sum_{K=0}^{NEL-1} \frac{\partial \Pi_{\text{int}}^K}{\partial \mathbf{x}_I} + \sum_{K=0}^{NEL-1} \frac{\partial \Pi_{\text{ext}}^K}{\partial \mathbf{x}_I} + \sum_{K=0}^{NP} \lambda_K \frac{\partial [\mathbf{t}_1^K \times \mathbf{t}_2^K]}{\partial \mathbf{x}_I} \cdot \mathbf{w}_K \\ \sum_{K=0}^{NEL-1} \frac{\partial \Pi_{\text{int}}^K}{\partial \mathbf{w}_I} + \sum_{K=0}^{NEL-1} \frac{\partial \Pi_{\text{ext}}^K}{\partial \mathbf{w}_I} + \lambda_I [\mathbf{t}_1^I \times \mathbf{t}_2^I] \\ [\mathbf{t}_1^I \times \mathbf{t}_2^I] \cdot \mathbf{w}_I \end{pmatrix} = \mathbf{0} \quad (44)$$

where λ_I are the NP Lagrange parameters. There is one Lagrange parameter per vertex so that the total number of Lagrange parameters is equal to the number of mesh vertices NP .

5.2.2. Local shear vector in convective coordinates The shear vector at node I can be expressed in the convective coordinate frame defined by the nodal tangent vectors \mathbf{t}_1^I and \mathbf{t}_2^I of the limit surface

$$\mathbf{w}_I = w^1_I \mathbf{t}_1^I + w^2_I \mathbf{t}_2^I \quad (45)$$

The shear vector in the interpolation equation (39c) and discrete equilibrium equations (40) can be interpreted in the sense of (45). In that case, there is no need for an additional constraint equation. The resulting discretized shell equations have as unknowns the two local shear vector components and the three displacements of the mid-surface. The derivation of the corresponding internal force vector and the stiffness matrix can be found in the appendix.

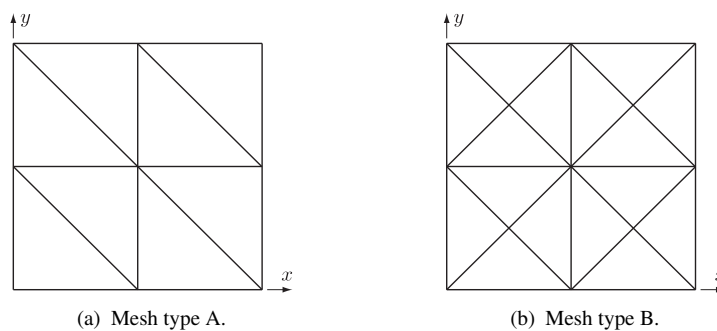


Figure 6. Two coarse meshes used for the discretization of the plate. The refined meshes are obtained through refinement by quadrisection of each triangle.

6. Examples

We evaluate the performance of the subdivision shells with the proposed shell kinematics using linear and geometrically nonlinear examples. First, the focus is on geometrically linear examples to emphasise the seamless transition from the Reissner-Mindlin to the Kirchhoff-Love shell model regime which is intrinsically present in the proposed approach. Secondly, the pinched cylinder example shows the applicability of the proposed elements to geometrically nonlinear problems.

6.1. Square plate

Square plates of different slenderness ratios and with either simply supported or clamped boundaries are subjected to uniformly distributed loading. The length of the plate is $L = 10$, the Young's modulus is $E = 1.092 \cdot 10^6$ and the Poisson's ratio is $\nu = 0.3$. As shown in Figure 6, two different types of meshes, referred to as type A and type B, are considered. The type B mesh contains five irregular domain vertices with a valence different from six; whereas the type A mesh contains no irregular domain vertices. The refined meshes are obtained by repeated quadrisection of the initial meshes, whereby each refinement step subdivides a triangle into four smaller triangles.

6.1.1. Thin plate with slenderness ratio $L/\bar{t} = 10^6$ In order to investigate the convergence of the proposed elements in case of extremely thin plates we consider a plate with a slenderness ratio of $L/\bar{t} = 10^6$ is considered. This is a challenging test case for conventional shear-flexible shell finite elements because of their propensity to shear locking. Shear locking can be understood as the inability of representing zero out-of-plane shear deformations in case of non-zero deflections. As well known in engineering, in particular for plates with a high slenderness ratio, the out-of-plane shear deformations are negligible. This implies that the shear-rigid Kirchhoff solution is a good approximation to the deformation and stress state in the three-dimensional plate.

The considered plate is computed with clamped as well as simply supported boundary conditions using one, three and seven Gauss quadrature points per element. The convergence of the error in the maximum deflection is plotted in Figure 7. The error in the numerical solution is determined with the analytical Kirchhoff series solution of the simply supported plate $0.00406235266065 \cdot L^4/D$ and the solution of the clamped plate $0.001265319087 \cdot L^4/D$ [31, 30], where D is the flexural stiffness

$$D = \frac{E\bar{t}^3}{12(1-\nu^2)} \quad (46)$$

Overall, the clamped plate solution is less accurate than the simply supported plate solution because of the more pronounced boundary effects. The actual convergence rate for the three and five point integration is approximately two and is in good agreement with the theoretical expected rate NP^{-2} [29]. In the used Loop subdivision shape functions the degree of the complete polynomials is three. Although one point integration does not lead to rank-deficient system matrices, the corresponding results show sub-optimal convergence. A possible reason for this is the method's inability to resolve the strong gradients present in the vicinity of the plate corners. In Figure 8, the convergence of the error in the strain energy for the clamped plate is plotted. According to Taylor et al. [30], the

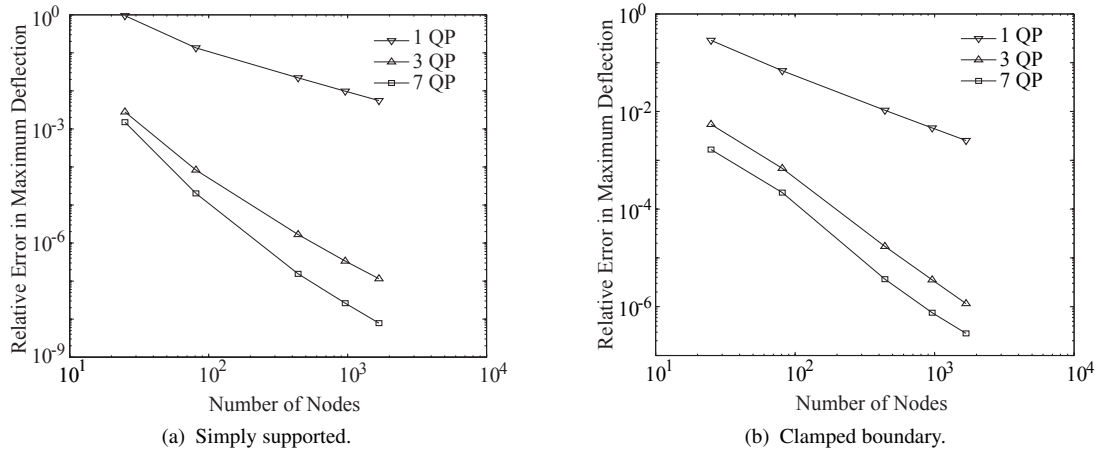


Figure 7. Thin plate with $L/\bar{t} = 10^6$ discretized with mesh type A. Convergence of the maximum deflection.

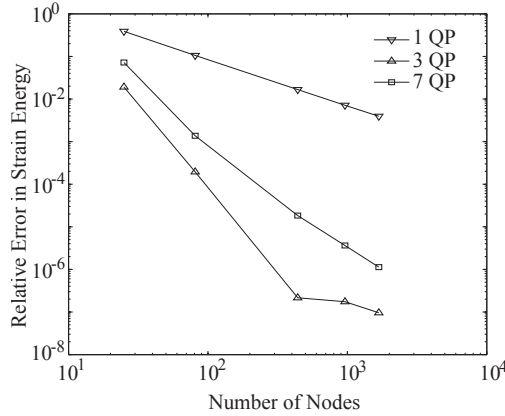


Figure 8. Convergence of the internal energy of the clamped plate with $L/\bar{t} = 10^6$ and discretized with mesh type A.

exact strain energy of the Kirchhoff solution is $0.0003891200775 \cdot L^4/D$. Again, one point integration shows a sub-optimal performance, whereas the solutions with three and seven quadrature points converge significantly faster. The convergence rate of the three quadrature point solution is close to the theoretical expected rate NP^{-2} [29]. The flattening out of the three quadrature point convergence curve can be explained with the inherent differences between the Kirchhoff reference solution and the shear-flexible numerical solution. In order to assess the true convergence of the presented method it is necessary to compute the error in the strain energy with respect to the shear-flexible analytic solution.

The convergence of the out-of-plane shear resultant along the plate centre and along the boundary are plotted in Figures 9 and 10, respectively. As can be seen in Figure 10(a), at the corners of the simply supported plate the shear resultant exhibits a singularity which represents the Kelvin-Kirchhoff edge resultant force. The asymmetry present in Figure 10 is an artefact of the plotting software used. It is worth emphasising that in the proposed shell model out-of-plane shear deformations and stress resultants are directly considered. The shear stress resultant is computed using the out-of-plane shear strains (6b) and the internal energy density (35). This is in stark contrast to the Kirchhoff theory where the out-of-plane shear resultant can only be determined using the equilibrium equations.

The convergence of the moments along the plate centre are plotted in Figure 11. For the simply supported case, the Kirchhoff model yields a maximum moment of 4.79 [31], which agrees well with the converged result. The computed moment does not exactly decay to zero at the boundary because the stress resultants are evaluated and plotted as element-wise constant. For the clamped case, the Kirchhoff model yields a clamping moment of 5.13 and a sagging

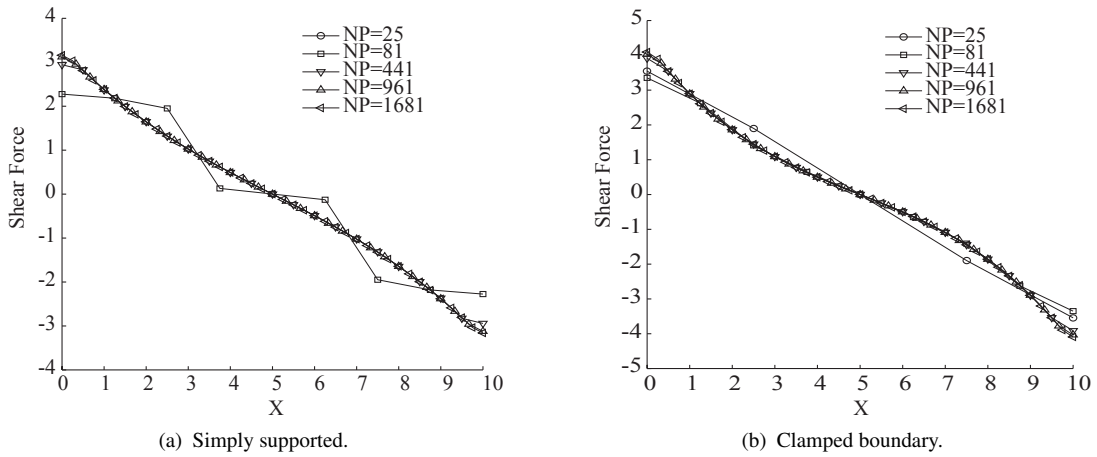


Figure 9. Thin plate with $L/\bar{t} = 10^6$ discretized with mesh type A. Convergence of the out-of-plane shear force along the centre line.

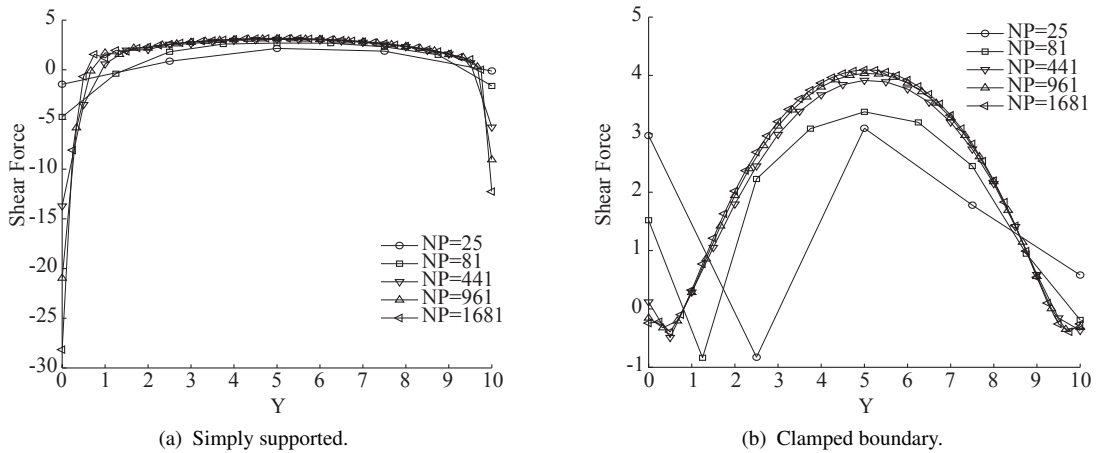


Figure 10. Thin plate with $L/\bar{t} = 10^6$ discretized with mesh type A. Convergence of the out-of-plane shear force along the boundary.

moment of 2.31 [31], which agree well with the converged results.

6.1.2. Thick plates In our second set of examples, the convergence of the proposed shell model in case of thick plates is investigated. The two considered plates have slenderness ratios of $L/\bar{t} = 5$ and $L/\bar{t} = 7.1429$. In the considered slenderness regime the out-of-plane shear deformations and the corresponding energies cannot be neglected. In Table II, the analytic solutions obtained using the three-dimensional linear elasticity equations and the Kirchhoff model are tabulated [27]. Depending on the slenderness ratio and boundary conditions, the error in the Kirchhoff solution is between 16.9% and 41.0%. In all cases the analytic solutions obtained with the Kirchhoff model are smaller than the ones obtained with the elasticity equations. As to be expected, the Kirchhoff model is inadequate for plates with relatively low slenderness ratios.

In Table III, the results of all our numerical computations are collected. In the simply supported case only the boundary displacements, i.e. $\mathbf{x} - \bar{\mathbf{x}} = \mathbf{0}$, are prescribed, and in the clamped case in addition to the boundary displacements the boundary rotations $\mathbf{a}_1 \times \mathbf{a}_2 + \mathbf{w} = \mathbf{0}$ are prescribed. For prescribing the rotations at the domain boundaries Lagrange parameters are used. The clamped boundary conditions correspond to the so-called clamped hard support boundary conditions in conventional shear-deformable plate theories. The tabulated relative errors are

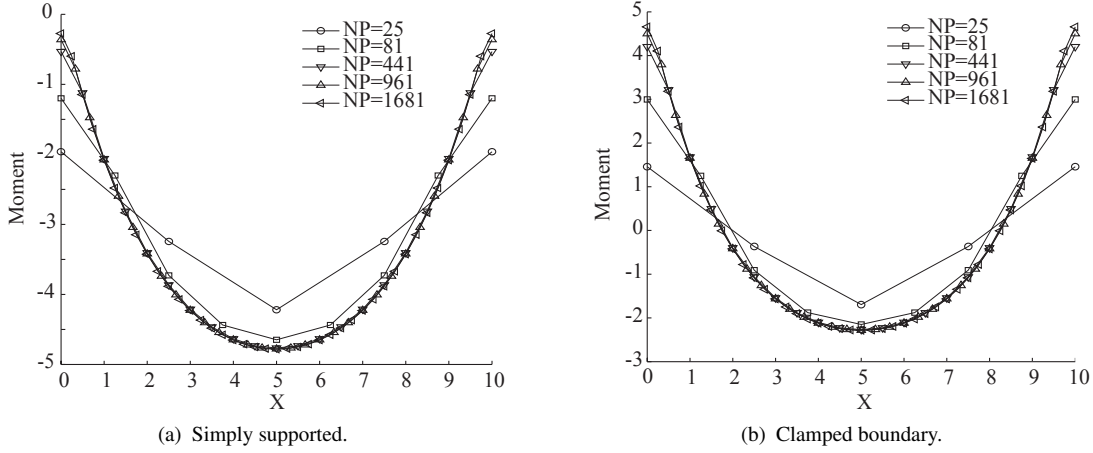


Figure 11. Thin plate with $L/\bar{t} = 10^6$ discretized with mesh type A. Convergence of the moment along the centre line.

	simply supported		clamped	
	$L/\bar{t} = 5$	$L/\bar{t} = 7.1429$	$L/\bar{t} = 5$	$L/\bar{t} = 7.1429$
elasticity solution	$6.7686 \cdot 10^{-5}$	$1.7807 \cdot 10^{-4}$	$2.6686 \cdot 10^{-5}$	$6.2133 \cdot 10^{-5}$
Kirchhoff solution	$5.0781 \cdot 10^{-5}$	$1.4805 \cdot 10^{-4}$	$1.5752 \cdot 10^{-5}$	$4.5933 \cdot 10^{-5}$
Kirchhoff model error	25.0%	16.9%	41.0%	26.1%

Table II. Thick plates with $L/\bar{t} = 5$ and $L/\bar{t} = 7.1429$. Comparison of the analytic maximum deflections obtained with three-dimensional elasticity and shear-rigid Kirchhoff model [27].

		simply supported		clamped	
		$L/\bar{t} = 5$	$L/\bar{t} = 7.1429$	$L/\bar{t} = 5$	$L/\bar{t} = 7.1429$
mesh type A	1 QP	2.96%	1.92%	26.36%	24.53%
	3 QP	1.78%	0.83%	0.48%	0.25%
	7 QP	1.77%	0.82%	0.48%	0.24%
mesh type B	1 QP	2.25%	1.13%	17.93%	17.95%
	3 QP	1.48%	0.52%	0.40%	0.19%
	7 QP	1.39%	0.44%	0.38%	0.17%

Table III. Thick plates with $L/\bar{t} = 5$ and $L/\bar{t} = 7.1429$. Error in the converged maximum deflection of the shear-flexible subdivision shell solution.

computed using the respective analytic three-dimensional solutions given in Srinivas et al. [27]. In the computations two different types of meshes are used: namely type A and type B meshes as shown in Figure 6. Overall, the results obtained with the shear-flexible subdivision shells are substantially more accurate than the corresponding solutions obtained with the Kirchhoff model. As in the thin-plate case, the use of one point integration leads to sub-optimal convergence and, hence, is not advisable for practical computations (see also Section 6.1.1). The numerical results obtained with three and seven quadrature points converge significantly faster than the one-point quadrature results.

Figures 12 and 13 show the convergence of the error in the maximum deflection for different combinations of mesh types, slenderness ratios and boundary conditions. Note that the errors are computed with respect to the analytic three-dimensional solution. Therefore, the given convergence plots are not suitable for extracting the convergence rate

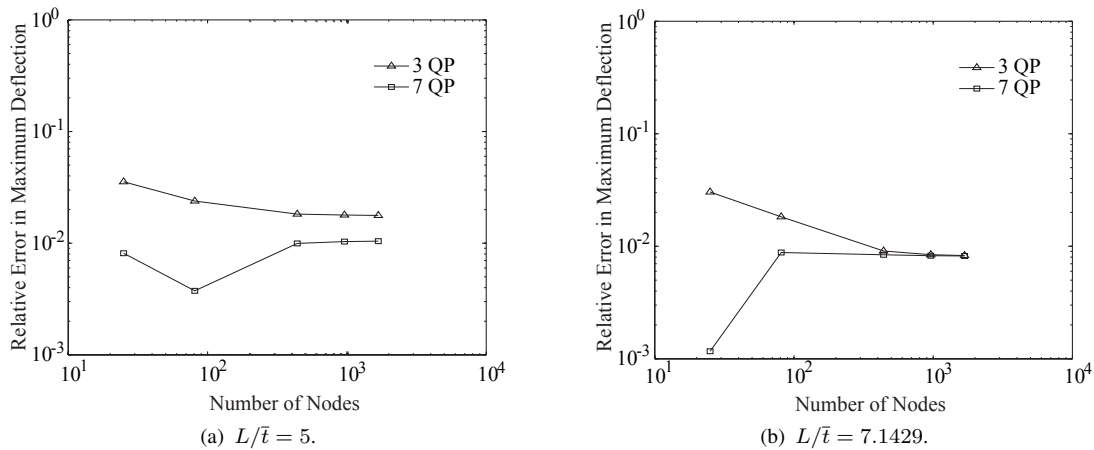


Figure 12. Simply supported thick plates discretized with mesh type A. Convergence of the relative error in maximum deflection. The relative errors are computed with respect to the corresponding analytical three-dimensional solutions.

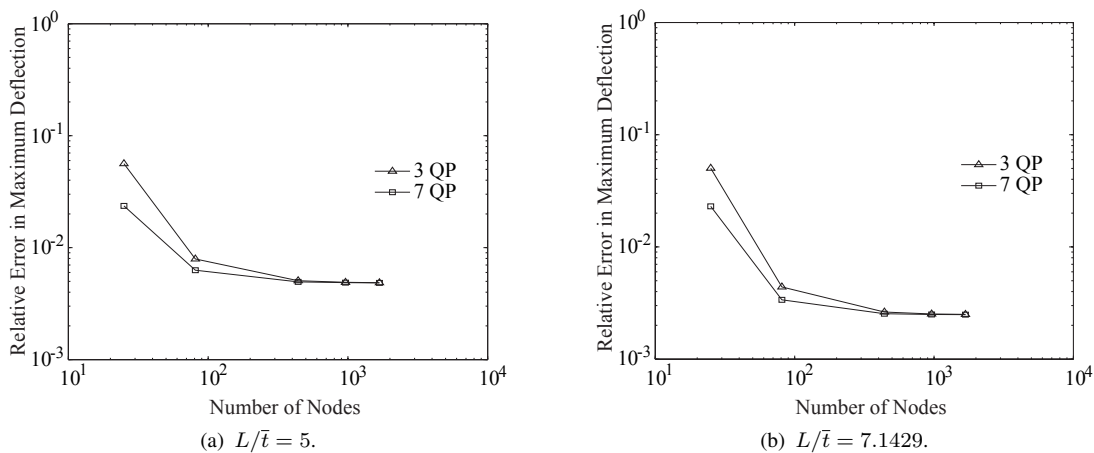


Figure 13. Clamped thick plates discretized with mesh type A. Convergence of the relative error in maximum deflection. The relative errors are computed with respect to the corresponding analytical three-dimensional solutions.

of the method. As can be deduced from the convergence plots the shear-flexible subdivision shells are able to provide highly accurate results with relatively coarse meshes. It is evident from the analytic results in Table II that the standard shear-rigid subdivision shells are inadequate.

In Figures 16 and 17, the convergence of the out-of-plane shear resultants are given for a simply supported and clamped plate. The two plots in Figure 16 are for the shear resultant along the centre of the plate, and the two plots in Figure 17 are for the shear resultants along the boundary of the plate. For the sake of brevity, only the results for the plate with $L/\bar{t} = 5$ have been included. Similar to thin plates, in the simply supported case the shear forces are focused at the corners. The corresponding shear forces in the clamped case vanish at the corners. Furthermore, the maximum shear resultant at the corners of the simply supported plate are smaller than corresponding values of a thin plate. In this context, it is worth recalling that the stress resultants of a Kirchhoff plate are independent of the plate thickness.

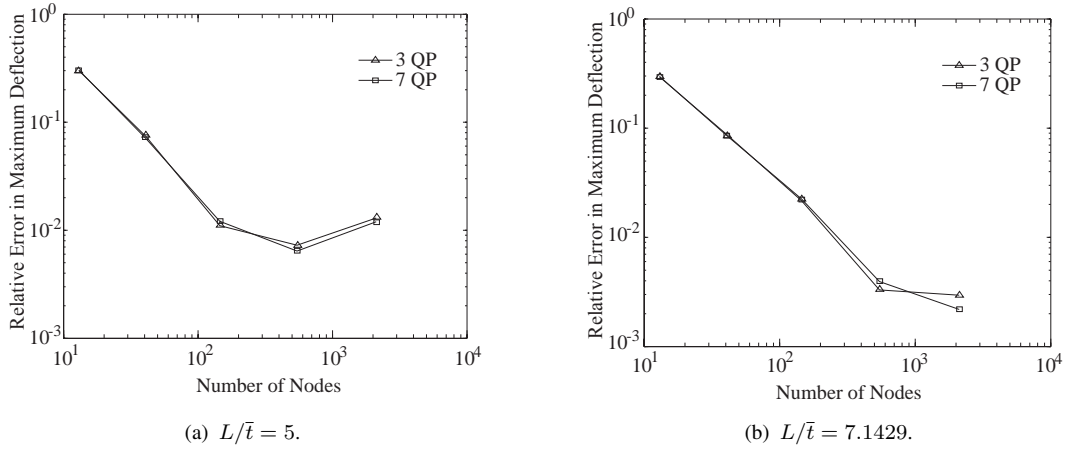


Figure 14. Simply supported thick plates discretized with mesh type B. Convergence of the relative error in maximum deflection. The relative errors are computed with respect to the corresponding analytical three-dimensional solutions.

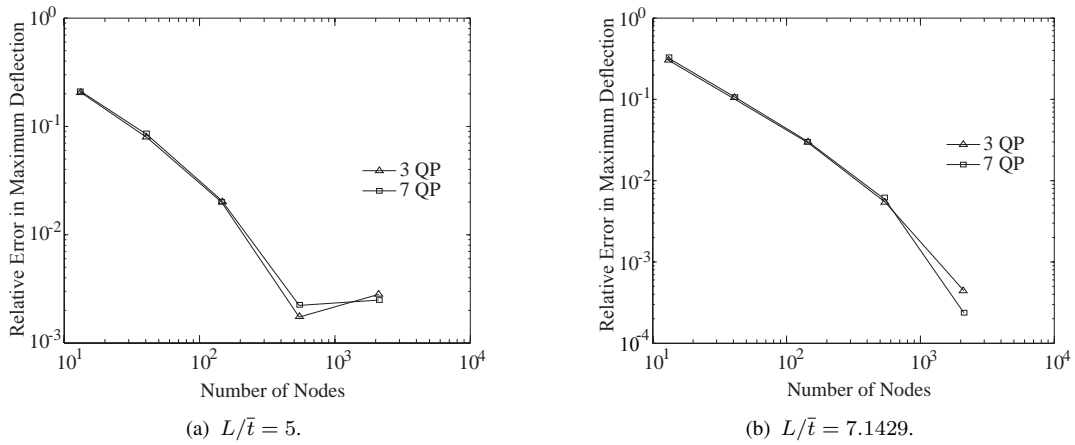


Figure 15. Clamped thick plates discretized with mesh type B. Convergence of the relative error in maximum deflection. The relative errors are computed with respect to the corresponding analytical three-dimensional solutions.

6.2. Circular plate

A uniformly loaded circular plate is considered for comparing the introduced shear-flexible subdivision shells with other plate finite elements. The radius of the plate is $R = 5$, the thickness is $h = 0.01$, Young's modulus is $E = 10.92 \cdot 10^6$ and Poisson's ratio is $\nu = 0$. The boundary conditions are clamped hard support. The analytic solution for this rotationally symmetric example can be found, e.g., in Timoshenko et al. [31]. The analytically obtained maximum deflection is 10.731 and the strain energy is 140.474.

A representative coarse finite element mesh used in the computations is shown in Figure 18. The relative error in the maximum deflection with three point quadrature versus the number of nodes is plotted in Figure 19(a). Furthermore, Figure 19(a) contains the results for the Xu [33] and MITC7 [1] elements, which have been extracted from [6]. Both elements are triangular and are based on the conventional shear-flexible Reissner-Mindlin model. According to Figure 19(a), the accuracy of the introduced shear-flexible shell is comparable to the Xu element and better than the MITC7 element. The convergence of the error in the strain energy is plotted in Figure 19(b).

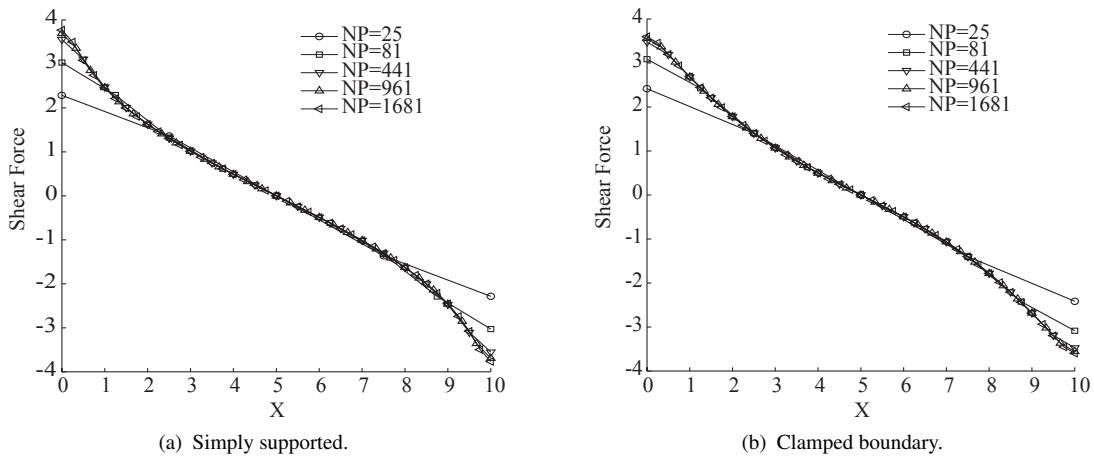


Figure 16. Thick plate with $L/\bar{t} = 5$ discretized with mesh type A. Convergence of the out-of-plane shear force along the centre line.

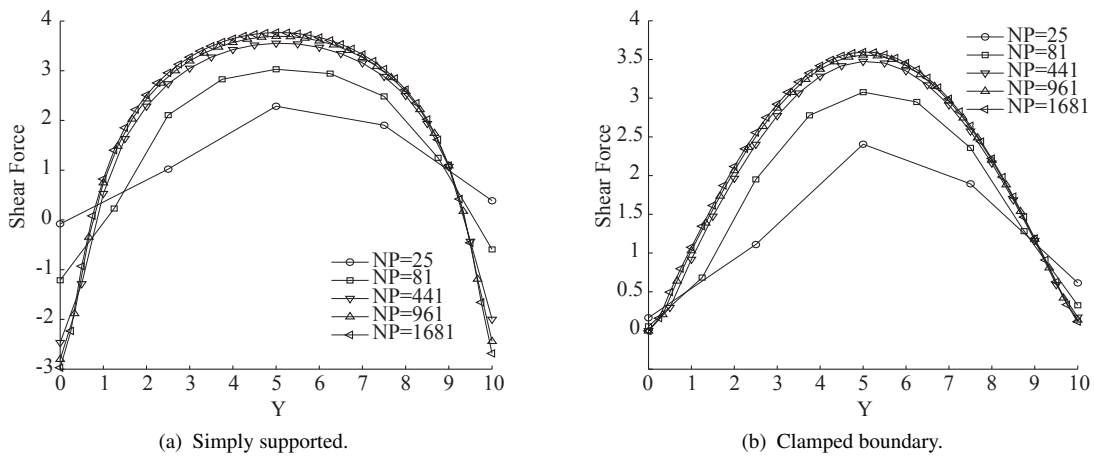


Figure 17. Thick plate with $L/\bar{t} = 5$ discretized with mesh type A. Convergence of the out-of-plane shear force along the boundary.

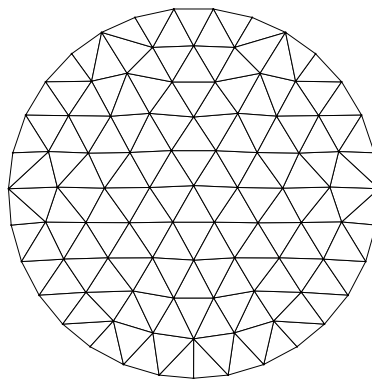


Figure 18. A representative mesh used in the computations.

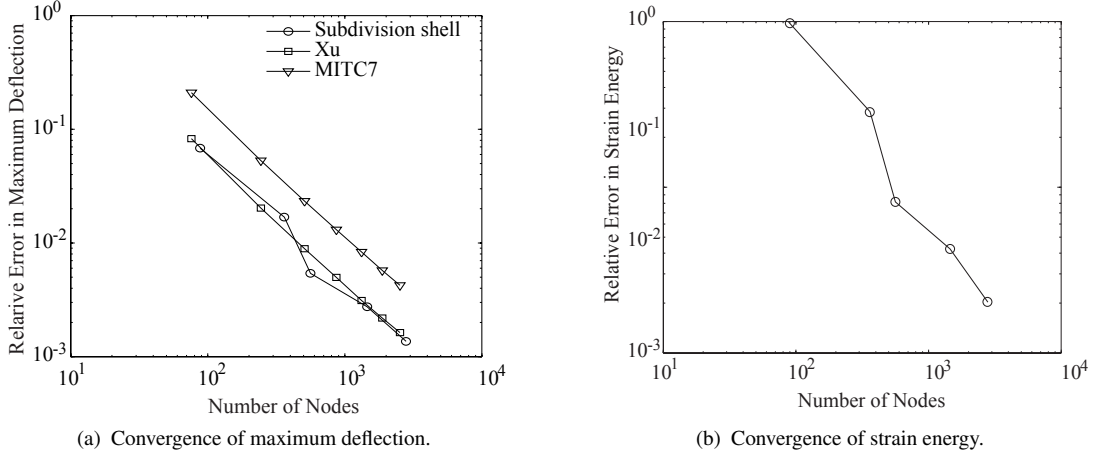


Figure 19. Circular plate.

6.3. Pinched cylinder

The pinched cylinder is a well studied problem and is part of the original shell obstacle course proposed by Belytschko et al. [2]. The cylinder is loaded with two diametrically opposing unit loads in its middle section. The displacements and rotations on its both edges are unconstrained. The length of the cylinder is $L = 600$; the radius is $R = 300$; the Young's modulus is $E = 3 \times 10^6$; and the Poisson's ratio is $\nu = 0.3$.

The cylindrical shell is a developable surface and can deform in the thin limit without any significant bending moments. The corresponding analytic membrane series solution can be found, e.g., in [31], which agrees for thin shells ($R/\bar{t} \gtrsim 100$) very well with the numerical Kirchhoff-Love solution [11]. According to Timoshenko et al. [31], the maximum increase in the diameter is

$$u_{\max} = \frac{2R^3}{\pi DL} \sum_{n=2,4,6,\dots} \frac{1}{(n^2-1)^2} \approx 0.149 \frac{R^3}{2DL} \quad (47)$$

and the maximum shortening in the diameter is

$$u_{\min} = \frac{2R^3}{\pi DL} \sum_{n=2,4,6,\dots} \frac{(-1)^{n/2+1}}{(n^2-1)^2} \approx 0.137 \frac{R^3}{2DL} \quad (48)$$

where the flexural stiffness D is as defined in (46). In the subsequent numerical comparisons $n = 200$ terms of both series solutions are used.

To study the approximation quality of the proposed shear-flexible shell model, we computed cylinders with a slenderness ranging from $R/\bar{t} = 7.5$ to $R/\bar{t} = 100$. In Figure 20 the used mesh with 1260 vertices and a representative deformed limit surface are shown.

In addition to the computations with the proposed shear-flexible shell model, three-dimensional solid computations with approximately 280000 ten-node tetrahedral elements have been performed. In all the three-dimensional computations six elements across the shell thickness are used. In Figure 21, the results of the proposed shell model and three-dimensional computations are plotted. Figure 21(a) depicts the maximum increase in the diameter occurring at the loading point. Since point loads lead to infinite displacements in three-dimensional elasticity, in Figure 21(a) only the displacements for the shear-flexible shell are plotted. Moreover, the shear-flexible solution is normalised with respect to the membrane solution (47), which is only accurate for sufficiently thin shells. For thicker shells the membrane solution (47) is smaller than the shear-flexible solution. The maximum shortening of the diameter occurring at the cylinder ends is plotted in Figure 21(b). The computed solutions for the shear-flexible shell as well as three-dimensional elasticity are included. In general, the shear flexible solution is slightly smaller than the three-dimensional elasticity solution. Overall, the comparison between the shell and elasticity solutions confirm that the proposed shear-flexible shell model approximates three-dimensional elasticity better than the conventional Kirchhoff-Love model.

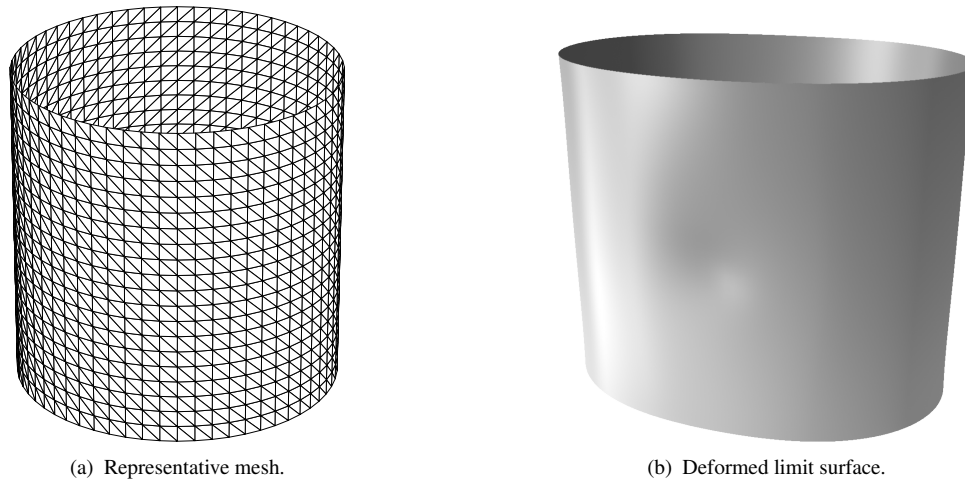


Figure 20. Pinched cylinder.

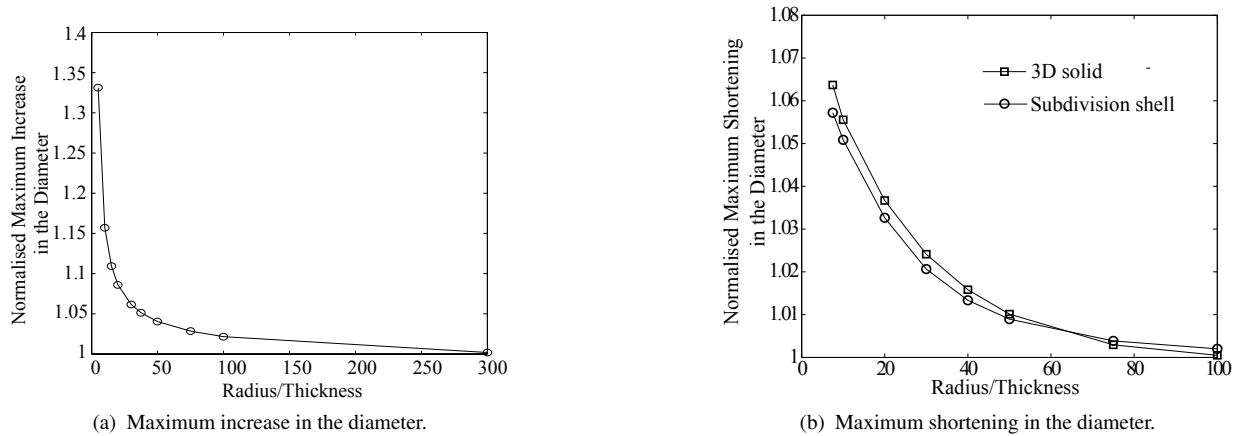


Figure 21. Pinched cylinder.

6.4. Pinched hemisphere

We consider the classical example of a hemispherical shell loaded by four point loads acting on its edge [11]. The radius of the hemisphere is 10; the Young's modulus is 6.825×10^7 ; and the Poisson's ratio is 0.3. On the edge of the shell the displacements and rotations are unconstrained. The applied loads have a magnitude of 2 and define two pairs of diametrically opposite loads alternating at 90° . The slenderness (R/\bar{t}) ranges from 7.5 to 250. In particular for slender hemispheres, the deformed shell exhibits almost no membrane strains so this example tests the elements ability to represent inextensional deformations.

The initial control mesh of the hemisphere is shown in Figure 22(a). The mesh finally used in the computations has 2113 nodes and is obtained by refining the initial control mesh by successive quadrisection and projecting the new vertices onto the sphere surface. Figure 22(b) shows the computed deformed limit surface of the $\bar{t} = 0.04$ thick hemisphere. In addition to the shell model, a three-dimensional solid model is considered with approximately 180000 ten-node tetrahedral elements. In the discretization of the solid model six elements across the shell thickness are used. The maximum displacement of the shear-flexible shell solution is plotted normalised with respect to the three-dimensional solid solution in Figure 23. As evident, for increasingly thinner hemispheres the shear-flexible shell solution converges towards the solid solution. For thicker hemispheres, the shear-flexible solution can be considered up to slenderness ratios of $R/\bar{t} \approx 20$ to be sufficiently accurate for most engineering applications.

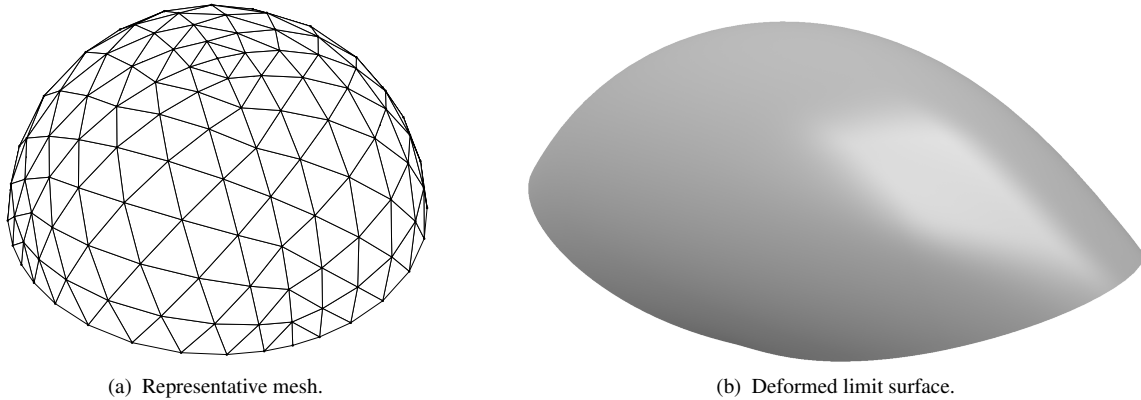


Figure 22. Pinched hemisphere.

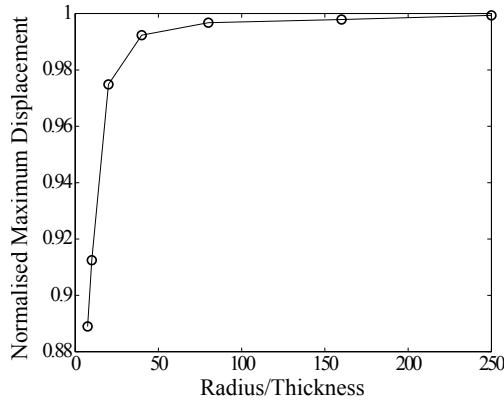


Figure 23. Pinched hemisphere. Maximum displacement of the shell solution normalised with respect to three-dimensional elasticity solution.

6.5. Nonlinear pinched cylinder

The geometrically nonlinear analysis of a pinched cylinder illustrates the performance of the proposed shear-flexible subdivision shells in case of large deformations. The deformed cylinder exhibits large inextensional bending deformations and a complex membrane state, c.f. Figure 25. The length of the cylinder is 10.35; the radius is 4.953; the thickness is 0.094; the Young's modulus is 10.5×10^6 ; and the Poisson's ratio is 0.3125. The cylinder is loaded by two diametrically opposing loads in its middle section and at its both ends the displacements and rotations are unconstrained (see Figure 24(a)). The cylinder has a slenderness ratio of $R/\bar{t} = 52.69$, which lies in the thin-thick transition regime, and it can be expected that the consideration of transverse shear is not crucial.

The cylinder is discretized with a regular mesh consisting of 840 nodes and 1600 elements, which matches the mesh used by Peric et al. [20]. In Figure 24(b), the load-displacement curves computed with the present method are compared with the results of Gruttmann et al. [15], Peric et al. [20] and Sansour [24]. The load-displacement curves are for the points A and B as indicated in Figure 24(a). As evident from Figure 24(b), the load-displacement curves computed with the shear-flexible subdivision shells are within the range provided by the three reference solutions.

7. Conclusions

We proposed a new shell model and introduced its discretization with subdivision shape functions. The kinematics of the proposed model can be considered as a special parameterisation of the conventional Reissner-Mindlin kinematics. The unknown variables are the position vector of the deformed mid-surface and the shear vector for describing the

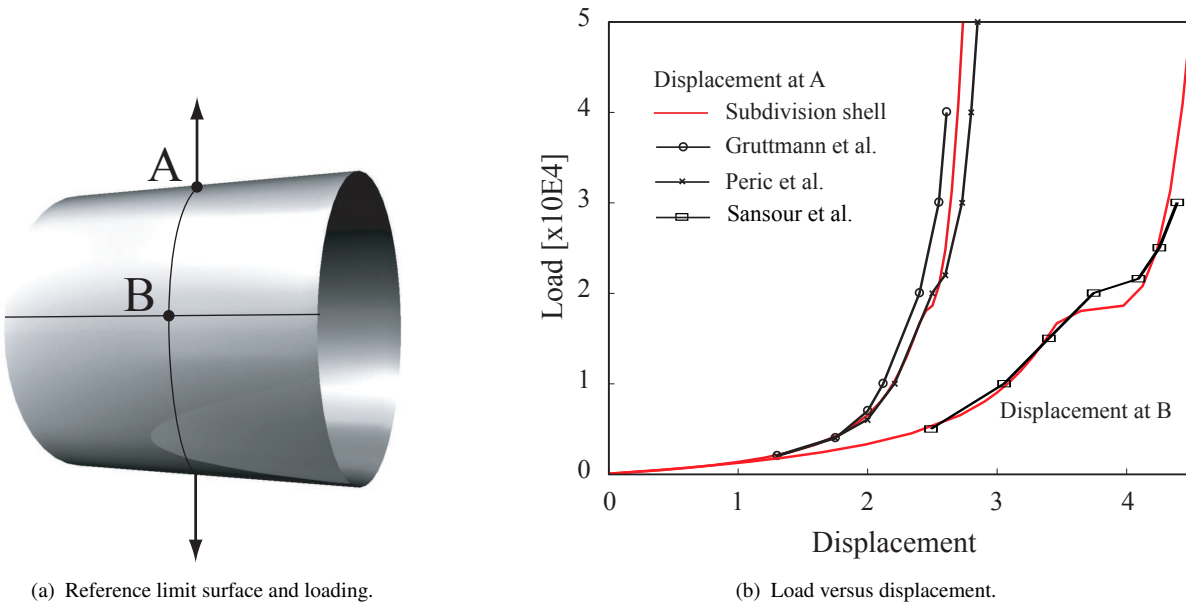


Figure 24. Nonlinear pinched cylinder.

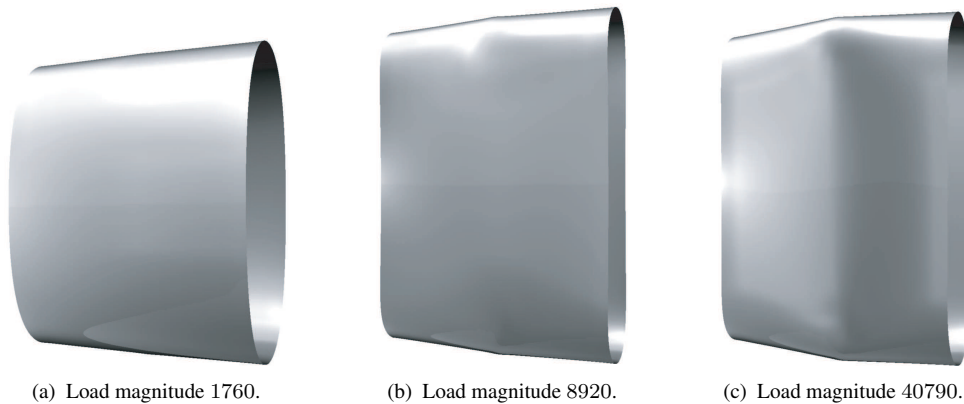


Figure 25. Nonlinear pinched cylinder. Sequence of deformed limit surfaces at increasing load values.

director deformation. The shear vector is a vector with two unknown components and is constrained to lie on the tangent plane of the mid-surface. The reference and deformed mid-surface and the shear-vector are interpolated using smooth subdivision shape functions. Thereby, the standard Rayleigh-Ritz formalism is used without resorting to any auxiliary techniques to treat shear-locking. The new shell elements, referred to as shear-flexible subdivision shells, are suitable for computing thin as well as thick shells. The convergence and quality of the computed displacement and stress fields is insensitive with respect to the shell thickness.

Another advantage of the developed subdivision shells is that subdivision surfaces are widely used in computer graphics and are an upcoming technology in computer aided design. As a result, subdivision surfaces provide an ideal isogeometric representation framework for analysis and geometric modelling [12]. Moreover, there is already a large body of work in computer graphics on efficient representation and processing of subdivision surfaces, such as on mesh adaptivity [14] or Boolean operations [4], which can be directly utilised in analysis software.

APPENDIX

In this appendix, we provide a step-by-step derivation of the internal force vector and stiffness matrix of the proposed shell model with five degrees of freedom. Each node has as degrees of freedom three coordinates (or displacements) and two local components of the shear vector. First explicit expressions are provided for the derivatives of the mid-surface vectors, shell director and strain variables. Subsequently, these expressions are combined to yield the internal force vector. Last, the stiffness matrix of the shell is derived.

II. Mid-surface vector and shell director derivatives

According to equation (39b), within each element the current configuration of the mid-surface is interpolated with

$$\mathbf{x}(\theta^1, \theta^2) = N^I(\theta^1, \theta^2) \mathbf{x}_I = N^I \mathbf{I} \cdot \mathbf{x}_I = \mathbf{N}^I \cdot \mathbf{x}_I$$

where \mathbf{N}^I is a 3-by-3 diagonal matrix containing the shape functions N^I . Here and in the following, the summation over the nodal indices I has been omitted for brevity. The base vectors of the discretized mid-surface and their derivatives are computed with

$$\mathbf{a}_\alpha = \mathbf{x}_{,\alpha} = \mathbf{N}_{,\alpha}^I \cdot \mathbf{x}_I \quad \text{and} \quad \mathbf{a}_{\alpha,\beta} = \mathbf{x}_{,\alpha\beta} = \mathbf{N}_{,\alpha\beta}^I \cdot \mathbf{x}_I \quad (50)$$

Their differentiation with respect to the nodal positions yields

$$\frac{\partial \mathbf{a}_\alpha}{\partial \mathbf{x}_I} = \mathbf{x}_{,\alpha} = \mathbf{N}_{,\alpha}^I \quad \text{and} \quad \frac{\partial \mathbf{a}_{\alpha,\beta}}{\partial \mathbf{x}_I} = \mathbf{N}_{,\alpha\beta}^I \quad (51)$$

Next, the derivatives of the shell director with respect to the nodal degrees of freedom are considered. To write the subsequent derivations in a more compact form, we introduce a non-unit normal and its gradient

$$\mathbf{z} = \mathbf{a}_1 \times \mathbf{a}_2 = \mathbf{A}_1 \cdot \mathbf{a}_2 = -\mathbf{A}_2 \cdot \mathbf{a}_1 \quad (52)$$

$$\mathbf{z}_{,\beta} = \mathbf{a}_{1,\beta} \times \mathbf{a}_2 + \mathbf{a}_1 \times \mathbf{a}_{2,\beta} = \mathbf{A}_{1,\beta} \cdot \mathbf{a}_2 + \mathbf{A}_1 \cdot \mathbf{a}_{2,\beta} \quad (53)$$

where the matrices \mathbf{A}_α and $\mathbf{A}_{\alpha,\beta}$ are the skew-symmetric matrices of the vectors \mathbf{a}_α and $\mathbf{a}_{\alpha,\beta}$, respectively. We obtain for their derivatives with respect to the nodal positions

$$\frac{\partial \mathbf{z}}{\partial \mathbf{x}_I} = -\mathbf{A}_2 \cdot \mathbf{N}_{,1}^I + \mathbf{A}_1 \cdot \mathbf{N}_{,2}^I = \widehat{\mathbf{Z}}^I \quad (54)$$

$$\frac{\partial \mathbf{z}_{,\beta}}{\partial \mathbf{x}_I} = -\mathbf{A}_2 \cdot \mathbf{N}_{,1\beta}^I + \mathbf{A}_{1\beta} \cdot \mathbf{N}_{,2}^I + \mathbf{A}_1 \cdot \mathbf{N}_{,2\beta}^I - \mathbf{A}_{2\beta} \cdot \mathbf{N}_{,1}^I = \widehat{\mathbf{Z}}_{,\beta}^I \quad (55)$$

The shear vector is discretized with

$$\mathbf{w} = \sum_I N^I(\theta^1, \theta^2) \mathbf{t}_\gamma^I w^\gamma_I \quad (56)$$

The nodal tangent vectors \mathbf{t}_γ^J are determined according to (37) in which the superscript J indicates the node. As presented in (37), the tangent vectors \mathbf{t}_γ^J depend on the vertex co-ordinates $\mathbf{x}_{I(J)}$ of the neighbouring vertices. This relation is denoted with $\mathbf{t}_\gamma^J = \sum_I L_\gamma^{JI} \mathbf{x}_{I(J)}$ or in matrix notation $\mathbf{t}_\gamma^J = \mathbf{L}_\gamma^{JI} \cdot \mathbf{x}_I$ with constant $\mathbf{L}_\gamma^{JI} = L_\gamma^{JI} \mathbf{I}$ in which the J -wise neighbouring index $I(J)$ is replaced with its absolute index I . The shear vector \mathbf{w} can be written as

$$\mathbf{w} = \sum_I N^I \mathbf{t}_\gamma^I w^\gamma_I = \sum_I (N^I \mathbf{t}_\gamma^I \otimes \mathbf{t}^{\gamma I}) \cdot \mathbf{w}_I = \widetilde{\mathbf{W}}^I \cdot \mathbf{w}_I \quad (57)$$

where the two components of the nodal shear vector are addressed with $w^\gamma_I = \mathbf{t}^{\gamma I} \cdot \mathbf{w}_I$. The gradient of the shear vector is

$$\mathbf{w}_{,\beta} = \sum_I N_{,\beta}^I \mathbf{t}_\gamma^I w^\gamma_I = \sum_I (N_{,\beta}^I \mathbf{t}_\gamma^I \otimes \mathbf{t}^{\gamma I}) \cdot \mathbf{w}_I = \widetilde{\mathbf{W}}_{,\beta}^I \cdot \mathbf{w}_I \quad (58)$$

and its derivatives with respect to the nodal unknowns are

$$\frac{\partial \mathbf{w}}{\partial \mathbf{x}_I} = \sum_J w^\alpha_J N^J \mathbf{L}_\alpha^{JI} = \widehat{\mathbf{W}}^I \quad \text{and} \quad \frac{\partial \mathbf{w}}{\partial \mathbf{w}_I} = \widetilde{\mathbf{W}}^I \quad (59)$$

$$\frac{\partial \mathbf{w}_{,\beta}}{\partial \mathbf{x}_I} = \sum_J w^\alpha_J N_{,\beta}^J \mathbf{L}_\alpha^{JI} = \widehat{\mathbf{W}}_{,\beta}^I \quad \text{and} \quad \frac{\partial \mathbf{w}_{,\beta}}{\partial \mathbf{w}_I} = \widetilde{\mathbf{W}}_{,\beta}^I \quad (60)$$

Note that a hat indicates a matrix holding a derivative with respect to the nodal coordinates \mathbf{x}_I , while a tilde indicates a matrix holding a derivative with respect to nodal shear vector \mathbf{w}_I .

Furthermore, we define the non-unit director

$$\mathbf{v} = \mathbf{a}_1 \times \mathbf{a}_2 + \mathbf{w} = \mathbf{z} + \mathbf{w} \quad (61)$$

The derivative of \mathbf{v} and $\mathbf{v}_{,\beta}$ with respect to the nodal unknowns can be expressed using the definitions in equations (54), (55), (59) and (60)

$$\frac{\partial \mathbf{v}}{\partial \mathbf{x}_I} = \widehat{\mathbf{Z}}^I + \widehat{\mathbf{W}}^I = \widehat{\mathbf{V}}^I \quad \text{and} \quad \frac{\partial \mathbf{v}}{\partial \mathbf{w}_I} = \widetilde{\mathbf{W}}^I = \widetilde{\mathbf{V}}^I \quad (62)$$

$$\frac{\partial \mathbf{v}_{,\beta}}{\partial \mathbf{x}_I} = \widehat{\mathbf{Z}}_{,\beta}^I + \widehat{\mathbf{W}}_{,\beta}^I = \widehat{\mathbf{V}}_{,\beta}^I \quad \text{and} \quad \frac{\partial \mathbf{v}_{,\beta}}{\partial \mathbf{w}_I} = \widetilde{\mathbf{W}}_{,\beta}^I = \widetilde{\mathbf{V}}_{,\beta}^I \quad (63)$$

Here, the matrices $\widetilde{\mathbf{W}}^I$ and $\widetilde{\mathbf{W}}_{,\beta}^I$ are re-labelled to preserve the naming pattern in regard to derivatives to follow.

Next, we introduce an auxiliary vector

$$\mathbf{s}_\beta = \frac{\mathbf{v}_{,\beta}}{|\mathbf{v}|} \quad (64)$$

with the derivatives

$$\frac{\partial \mathbf{s}_\beta}{\partial \mathbf{x}_I} = \frac{1}{|\mathbf{v}|} \left[\widehat{\mathbf{V}}_{,\beta}^I - \mathbf{s}_\beta \otimes (\mathbf{d} \cdot \widehat{\mathbf{V}}^I) \right] = \widehat{\mathbf{S}}_\beta^I \quad (65)$$

$$\frac{\partial \mathbf{s}_\beta}{\partial \mathbf{w}_I} = \frac{1}{|\mathbf{v}|} \left[\widetilde{\mathbf{V}}_{,\beta}^I - \mathbf{s}_\beta \otimes (\mathbf{d} \cdot \widetilde{\mathbf{V}}^I) \right] = \widetilde{\mathbf{S}}_\beta^I \quad (66)$$

The auxiliary vector \mathbf{s}_β permits to, eventually, express the derivatives of the director and its gradient with respect to nodal degrees of freedom with

$$\frac{\partial \mathbf{d}}{\partial \mathbf{x}_I} = \frac{1}{|\mathbf{v}|} \left[\widehat{\mathbf{V}}^I - \mathbf{d} \otimes (\mathbf{d} \cdot \widehat{\mathbf{V}}^I) \right] = \widehat{\mathbf{D}}^I \quad (67)$$

$$\frac{\partial \mathbf{d}}{\partial \mathbf{w}_I} = \frac{1}{|\mathbf{v}|} \left[\widetilde{\mathbf{V}}^I - \mathbf{d} \otimes (\mathbf{d} \cdot \widetilde{\mathbf{V}}^I) \right] = \widetilde{\mathbf{D}}^I \quad (68)$$

and

$$\frac{\partial \mathbf{d}_{,\beta}}{\partial \mathbf{x}_I} = \left[\widehat{\mathbf{S}}_\beta^I - \mathbf{d} \otimes (\mathbf{s}_\beta \cdot \widehat{\mathbf{D}}^I + \mathbf{d} \cdot \widehat{\mathbf{S}}_\beta^I) - (\mathbf{d} \cdot \mathbf{s}_\beta) \widehat{\mathbf{D}}^I \right] = \widehat{\mathbf{D}}_{,\beta}^I \quad (69)$$

$$\frac{\partial \mathbf{d}_{,\beta}}{\partial \mathbf{w}_I} = \left[\widetilde{\mathbf{S}}_\beta^I - \mathbf{d} \otimes (\mathbf{s}_\beta \cdot \widetilde{\mathbf{D}}^I + \mathbf{d} \cdot \widetilde{\mathbf{S}}_\beta^I) - (\mathbf{d} \cdot \mathbf{s}_\beta) \widetilde{\mathbf{D}}^I \right] = \widetilde{\mathbf{D}}_{,\beta}^I \quad (70)$$

III. Strain derivatives

The derivatives of the membrane and bending strain components (6) with respect to the nodal degrees of freedom are expressed using the definitions of preceding Appendix II

$$\frac{\partial \alpha_{\alpha\beta}}{\partial \mathbf{x}_I} = \frac{1}{2} (\mathbf{a}_\beta \cdot \mathbf{N}_{,\alpha}^I + \mathbf{a}_\alpha \cdot \mathbf{N}_{,\beta}^I) = \widehat{\mathbf{a}}_{\alpha\beta}^I \quad (71a)$$

$$\frac{\partial \alpha_{\alpha 3}}{\partial \mathbf{x}_I} = \frac{\partial \alpha_{3\alpha}}{\partial \mathbf{x}_I} = \frac{1}{2} (\mathbf{d} \cdot \mathbf{N}_{,\alpha}^I + \mathbf{a}_\alpha \cdot \widehat{\mathbf{D}}^I) = \widehat{\mathbf{a}}_{\alpha 3}^I \quad (71b)$$

$$\frac{\partial \alpha_{\alpha 3}}{\partial \mathbf{w}_I} = \frac{\partial \alpha_{3\alpha}}{\partial \mathbf{w}_I} = \frac{1}{2} (\mathbf{a}_\alpha \cdot \widetilde{\mathbf{D}}^I) = \widetilde{\mathbf{a}}_{\alpha 3}^I \quad (71c)$$

$$\frac{\partial \beta_{\alpha\beta}}{\partial \mathbf{x}_I} = \frac{1}{2} (\mathbf{d}_{,\beta} \cdot \mathbf{N}_{,\alpha}^I + \mathbf{a}_\alpha \cdot \widehat{\mathbf{D}}_{,\beta}^I + \mathbf{d}_{,\alpha} \cdot \mathbf{N}_{,\beta}^I + \mathbf{a}_\beta \cdot \widehat{\mathbf{D}}_{,\alpha}^I) = \widehat{\mathbf{b}}_{\alpha\beta}^I \quad (71d)$$

$$\frac{\partial \beta_{\alpha\beta}}{\partial \mathbf{w}_I} = \frac{1}{2} (\mathbf{a}_\alpha \cdot \widetilde{\mathbf{D}}_{,\beta}^I + \mathbf{a}_\beta \cdot \widetilde{\mathbf{D}}_{,\alpha}^I) = \widetilde{\mathbf{b}}_{\alpha\beta}^I \quad (71e)$$

IV. Equilibrium equations and linearisation

Following equation (31), the discrete equilibrium equations (40) are recalled

$$\begin{bmatrix} \widehat{\mathbf{f}}_{\text{int}}^I(\mathbf{x}_J, \mathbf{w}_J) - \widehat{\mathbf{f}}_{\text{ext}}^I(\mathbf{x}_J, \mathbf{w}_J) \\ \widetilde{\mathbf{f}}_{\text{int}}^I(\mathbf{x}_J, \mathbf{w}_J) - \widetilde{\mathbf{f}}_{\text{ext}}^I(\mathbf{x}_J, \mathbf{w}_J) \end{bmatrix} = \mathbf{0} \quad (72)$$

in which a dependency of the internal and external nodal forces on the current configuration is indicated. However, in the following paragraphs the derivations of the external nodal forces are not considered.

The internal forces (27) can be expressed with the strain derivatives (71), i.e.

$$\widehat{\mathbf{f}}_{\text{int}}^I = \int_{\overline{\Omega}} \left(n^{\alpha\beta} \widehat{\mathbf{a}}_{\alpha\beta}^I + 2n^{\alpha 3} \widehat{\mathbf{a}}_{\alpha 3}^I + m^{\alpha\beta} \widehat{\mathbf{b}}_{\alpha\beta}^I \right) d\overline{\Omega} \quad (73)$$

$$\widetilde{\mathbf{f}}_{\text{int}}^I = \int_{\overline{\Omega}} \left(2n^{\alpha 3} \widetilde{\mathbf{a}}_{\alpha 3}^I + m^{\alpha\beta} \widetilde{\mathbf{b}}_{\alpha\beta}^I \right) d\overline{\Omega} \quad (74)$$

Likewise, the discretization of the expression of the external forces (30) yields

$$\widehat{\mathbf{f}}_{\text{ext}}^I = \int_{\overline{\Omega}} \left(\mathbf{p} \cdot \mathbf{N}^I + \mathbf{q} \cdot \widehat{\mathbf{D}}^I \right) d\overline{\Omega} + \int_{\overline{\Gamma}} \left(\mathbf{r} \cdot \mathbf{N}^I + \mathbf{s} \cdot \widehat{\mathbf{D}}^I \right) d\overline{\Gamma} \quad (75)$$

$$\widetilde{\mathbf{f}}_{\text{ext}}^I = \int_{\overline{\Omega}} \left(\mathbf{q} \cdot \widetilde{\mathbf{D}}^I \right) d\overline{\Omega} + \int_{\overline{\Gamma}} \left(\mathbf{s} \cdot \widetilde{\mathbf{D}}^I \right) d\overline{\Gamma} \quad (76)$$

The nodal equilibrium (72) is a set of nonlinear algebraic equations. Next, we proceed to the derivation of the corresponding stiffness matrix

$$\begin{bmatrix} \widehat{\mathbf{k}}^{IJ} & \widetilde{\mathbf{k}}^{IJ} \\ \widehat{\mathbf{k}}^{IJ} & \widetilde{\mathbf{k}}^{IJ} \end{bmatrix} = \begin{bmatrix} \frac{\partial \left(\widehat{\mathbf{f}}_{\text{int}}^I(\mathbf{x}_J, \mathbf{w}_J) - \widehat{\mathbf{f}}_{\text{ext}}^I \right)}{\partial \mathbf{x}_J} & \frac{\partial \left(\widehat{\mathbf{f}}_{\text{int}}^I(\mathbf{x}_J, \mathbf{w}_J) - \widehat{\mathbf{f}}_{\text{ext}}^I \right)}{\partial \mathbf{w}_J} \\ \frac{\partial \left(\widetilde{\mathbf{f}}_{\text{int}}^I(\mathbf{x}_J, \mathbf{w}_J) - \widetilde{\mathbf{f}}_{\text{ext}}^I \right)}{\partial \mathbf{x}_J} & \frac{\partial \left(\widetilde{\mathbf{f}}_{\text{int}}^I(\mathbf{x}_J, \mathbf{w}_J) - \widetilde{\mathbf{f}}_{\text{ext}}^I \right)}{\partial \mathbf{w}_J} \end{bmatrix} \quad (77)$$

The contribution of the internal forces to the stiffness matrix consists of

$$\begin{aligned} \frac{\partial \widehat{\mathbf{f}}_{\text{int}}^I}{\partial \mathbf{x}_J} &= \int_{\overline{\Omega}} \left(\widehat{\mathbf{a}}_{\alpha\beta}^I \otimes \frac{\partial n^{\alpha\beta}}{\partial \mathbf{x}_J} + 2\widehat{\mathbf{a}}_{\alpha 3}^I \otimes \frac{\partial n^{\alpha 3}}{\partial \mathbf{x}_J} + \widehat{\mathbf{b}}_{\alpha\beta}^I \otimes \frac{\partial m^{\alpha\beta}}{\partial \mathbf{x}_J} \right) d\overline{\Omega} \\ &+ \int_{\overline{\Omega}} \left(n^{\alpha\beta} \frac{\partial \widehat{\mathbf{a}}_{\alpha\beta}^I}{\partial \mathbf{x}_J} + 2n^{\alpha 3} \frac{\partial \widehat{\mathbf{a}}_{\alpha 3}^I}{\partial \mathbf{x}_J} + m^{\alpha\beta} \frac{\partial \widehat{\mathbf{b}}_{\alpha\beta}^I}{\partial \mathbf{x}_J} \right) d\overline{\Omega} \end{aligned} \quad (78a)$$

$$\begin{aligned} \frac{\partial \widehat{\mathbf{f}}_{\text{int}}^I}{\partial \mathbf{w}_J} &= \int_{\overline{\Omega}} \left(\widehat{\mathbf{a}}_{\alpha\beta}^I \otimes \frac{\partial n^{\alpha\beta}}{\partial \mathbf{w}_J} + 2\widehat{\mathbf{a}}_{\alpha 3}^I \otimes \frac{\partial n^{\alpha 3}}{\partial \mathbf{w}_J} + \widehat{\mathbf{b}}_{\alpha\beta}^I \otimes \frac{\partial m^{\alpha\beta}}{\partial \mathbf{w}_J} \right) d\overline{\Omega} \\ &+ \int_{\overline{\Omega}} \left(n^{\alpha\beta} \frac{\partial \widehat{\mathbf{a}}_{\alpha\beta}^I}{\partial \mathbf{w}_J} + 2n^{\alpha 3} \frac{\partial \widehat{\mathbf{a}}_{\alpha 3}^I}{\partial \mathbf{w}_J} + m^{\alpha\beta} \frac{\partial \widehat{\mathbf{b}}_{\alpha\beta}^I}{\partial \mathbf{w}_J} \right) d\overline{\Omega} \end{aligned} \quad (78b)$$

$$\frac{\partial \widetilde{\mathbf{f}}_{\text{int}}^I}{\partial \mathbf{x}_J} = \int_{\overline{\Omega}} \left(2\widetilde{\mathbf{a}}_{\alpha 3}^I \otimes \frac{\partial n^{\alpha 3}}{\partial \mathbf{x}_J} + \widetilde{\mathbf{b}}_{\alpha\beta}^I \otimes \frac{\partial m^{\alpha\beta}}{\partial \mathbf{x}_J} \right) d\overline{\Omega} + \int_{\overline{\Omega}} \left(2n^{\alpha 3} \frac{\partial \widetilde{\mathbf{a}}_{\alpha 3}^I}{\partial \mathbf{x}_J} + m^{\alpha\beta} \frac{\partial \widetilde{\mathbf{b}}_{\alpha\beta}^I}{\partial \mathbf{x}_J} \right) d\overline{\Omega} \quad (78c)$$

$$\frac{\partial \widetilde{\mathbf{f}}_{\text{int}}^I}{\partial \mathbf{w}_J} = \int_{\overline{\Omega}} \left(2\widetilde{\mathbf{a}}_{\alpha 3}^I \otimes \frac{\partial n^{\alpha 3}}{\partial \mathbf{w}_J} + \widetilde{\mathbf{b}}_{\alpha\beta}^I \otimes \frac{\partial m^{\alpha\beta}}{\partial \mathbf{w}_J} \right) d\overline{\Omega} + \int_{\overline{\Omega}} \left(2n^{\alpha 3} \frac{\partial \widetilde{\mathbf{a}}_{\alpha 3}^I}{\partial \mathbf{w}_J} + m^{\alpha\beta} \frac{\partial \widetilde{\mathbf{b}}_{\alpha\beta}^I}{\partial \mathbf{w}_J} \right) d\overline{\Omega} \quad (78d)$$

In case of a Saint Venant-Kirchhoff material, see Section 4, the derivatives of the stress resultants with respect to the nodal degrees of freedom take a particularly simple form

$$\begin{aligned} \frac{\partial n^{ij}}{\partial \mathbf{x}_J} &= \bar{t} C^{ijkl} \widehat{\mathbf{a}}_{kl}^J & \text{and} & \quad \frac{\partial n^{ij}}{\partial \mathbf{w}_J} = \bar{t} C^{ijkl} \widetilde{\mathbf{a}}_{kl}^J \\ \frac{\partial m^{ij}}{\partial \mathbf{x}_J} &= \frac{\bar{t}^3}{12} C^{ijkl} \widehat{\mathbf{b}}_{kl}^J & \text{and} & \quad \frac{\partial m^{ij}}{\partial \mathbf{w}_J} = \frac{\bar{t}^3}{12} C^{ijkl} \widetilde{\mathbf{b}}_{kl}^J \end{aligned} \quad (79)$$

To evaluate the stiffness matrix components (78), the second derivatives of the strain components with respect to the nodal degrees of freedom are needed, which are

$$2 \frac{\partial \hat{\mathbf{a}}_{\alpha\beta}^I}{\partial \mathbf{x}_J} = \mathbf{N}_{,\alpha}^I \cdot \mathbf{N}_{,\beta}^J + \mathbf{N}_{,\beta}^I \cdot \mathbf{N}_{,\alpha}^J \quad (80a)$$

$$2 \frac{\partial \hat{\mathbf{a}}_{\alpha 3}^I}{\partial \mathbf{x}_J} = \mathbf{N}_{,\alpha}^I \cdot \hat{\mathbf{D}}^J + \hat{\mathbf{D}}^I \cdot \mathbf{N}_{,\alpha}^J + \mathbf{a}_\alpha \cdot \hat{\hat{\mathbf{D}}}^{IJ} \quad (80b)$$

$$2 \frac{\partial \hat{\mathbf{b}}_{\alpha\beta}^I}{\partial \mathbf{x}_J} = \mathbf{N}_{,\alpha}^I \cdot \hat{\mathbf{D}}_{,\beta}^J + \hat{\mathbf{D}}_{,\beta}^I \cdot \mathbf{N}_{,\alpha}^J + \mathbf{a}_\alpha \cdot \hat{\hat{\mathbf{D}}}_{,\beta}^{IJ} \quad (80c)$$

$$+ \mathbf{N}_{,\beta}^I \cdot \hat{\mathbf{D}}_{,\alpha}^J + \hat{\mathbf{D}}_{,\alpha}^I \cdot \mathbf{N}_{,\beta}^J + \mathbf{a}_\beta \cdot \hat{\hat{\mathbf{D}}}_{,\alpha}^{IJ}$$

The mixed derivatives of the strain components with respect to the nodal coordinates and the shear vector are

$$2 \frac{\partial \hat{\mathbf{a}}_{\alpha 3}^I}{\partial \mathbf{w}_J} = \mathbf{N}_{,\alpha}^I \cdot \tilde{\mathbf{D}}^J + \mathbf{a}_\alpha \cdot \tilde{\tilde{\mathbf{D}}}^{IJ} \quad (80d)$$

$$2 \frac{\partial \hat{\mathbf{b}}_{\alpha\beta}^I}{\partial \mathbf{w}_J} = \mathbf{N}_{,\alpha}^I \cdot \tilde{\mathbf{D}}_{,\beta}^J + \mathbf{a}_\alpha \cdot \tilde{\tilde{\mathbf{D}}}_{,\beta}^{IJ} + \mathbf{N}_{,\beta}^I \cdot \tilde{\mathbf{D}}_{,\alpha}^J + \mathbf{a}_\beta \cdot \tilde{\tilde{\mathbf{D}}}_{,\alpha}^{IJ} \quad (80e)$$

$$2 \frac{\partial \tilde{\mathbf{a}}_{\alpha 3}^I}{\partial \mathbf{x}_J} = \tilde{\mathbf{D}}^{I\top} \cdot \mathbf{N}_{,\alpha}^J + \mathbf{a}_\alpha \cdot \hat{\hat{\mathbf{D}}}^{IJ} \quad (80f)$$

$$2 \frac{\partial \tilde{\mathbf{b}}_{\alpha\beta}^I}{\partial \mathbf{x}_J} = \tilde{\mathbf{D}}_{,\beta}^{I\top} \cdot \mathbf{N}_{,\alpha}^J + \mathbf{a}_\alpha \cdot \hat{\hat{\mathbf{D}}}_{,\beta}^{IJ} + \tilde{\mathbf{D}}_{,\alpha}^{I\top} \cdot \mathbf{N}_{,\beta}^J + \mathbf{a}_\beta \cdot \hat{\hat{\mathbf{D}}}_{,\alpha}^{IJ} \quad (80g)$$

Finally, the second derivatives of the strain components with respect to the nodal shear vector are

$$2 \frac{\partial \tilde{\mathbf{a}}_{\alpha 3}^I}{\partial \mathbf{w}_J} = \mathbf{a}_\alpha \cdot \tilde{\tilde{\mathbf{D}}}^{IJ} \quad (80h)$$

$$2 \frac{\partial \tilde{\mathbf{b}}_{\alpha\beta}^I}{\partial \mathbf{w}_J} = \mathbf{a}_\alpha \cdot \tilde{\tilde{\mathbf{D}}}_{,\beta}^{IJ} + \mathbf{a}_\beta \cdot \tilde{\tilde{\mathbf{D}}}_{,\alpha}^{IJ} \quad (80i)$$

In the preceding equations additional hat and tilde are used to denote second derivatives with respect to nodal positions and shear vectors, respectively. Importantly, the second derivatives of the unit-length thickness director and its covariant gradient, e.g. $\hat{\hat{\mathbf{D}}}^{IJ}$ and $\hat{\hat{\mathbf{D}}}_{,\beta}^{IJ}$, are both third-order tensors. In the equations (80), the third order tensors appear always multiplied with a vector. In the following derivations, we denote the additional vector with a dummy vector \mathbf{y} which in most cases represents a tangent base vector \mathbf{a}_α and in a few the thickness director \mathbf{d} .

To compute the second derivatives $\mathbf{y} \cdot \hat{\hat{\mathbf{D}}}^{IJ}$, $\mathbf{y} \cdot \hat{\hat{\mathbf{D}}}_{,\beta}^{IJ}$, etc., intermediate steps are taken to deal with the second derivatives of the auxiliary mid-surface vectors \mathbf{z} , \mathbf{v} and \mathbf{s}_β defined in Appendix II. The second derivative of the non-unit normal $\mathbf{z} = \mathbf{a}_1 \times \mathbf{a}_2$ and its gradient $\mathbf{z}_{,\beta}$ with respect to the nodal positions are

$$\mathbf{y} \cdot \hat{\hat{\mathbf{Z}}}^{IJ} = \mathbf{y} \cdot \frac{\partial \hat{\mathbf{Z}}^I}{\partial \mathbf{x}_J} = -\mathbf{N}_{,1}^I \cdot \mathbf{Y} \cdot \mathbf{N}_{,2}^J + \mathbf{N}_{,2}^I \cdot \mathbf{Y} \cdot \mathbf{N}_{,1}^J \quad (81)$$

$$\mathbf{y} \cdot \hat{\hat{\mathbf{Z}}}_{,\beta}^{IJ} = \mathbf{y} \cdot \frac{\partial \hat{\mathbf{Z}}_{,\beta}^I}{\partial \mathbf{x}_J} = -\mathbf{N}_{,1\beta}^I \cdot \mathbf{Y} \cdot \mathbf{N}_{,2}^J + \mathbf{N}_{,2}^I \cdot \mathbf{Y} \cdot \mathbf{N}_{,1\beta}^J$$

$$+ \mathbf{N}_{,2\beta}^I \cdot \mathbf{Y} \cdot \mathbf{N}_{,1}^J - \mathbf{N}_{,1}^I \cdot \mathbf{Y} \cdot \mathbf{N}_{,2\beta}^J$$

in which \mathbf{Y} is the skew-symmetric matrix of the dummy vector \mathbf{y} , i.e. $\mathbf{Y} \cdot \mathbf{c} = \mathbf{y} \times \mathbf{c}$.

The second derivatives of the shear vector \mathbf{w} with respect to the nodal degrees of freedom are given by

$$\mathbf{y} \cdot \hat{\hat{\mathbf{W}}}^{IJ} = \mathbf{0} \quad \text{and} \quad \mathbf{y} \cdot \hat{\hat{\mathbf{W}}}^{IJ} = (\mathbf{N}^J \mathbf{y} \cdot \mathbf{L}_\gamma^{JI}) \otimes \mathbf{t}^{\gamma J} \quad (82)$$

$$\mathbf{y} \cdot \hat{\hat{\mathbf{W}}}^{IJ} = \mathbf{t}^{\gamma I} \otimes (\mathbf{N}^I \mathbf{y} \cdot \mathbf{L}_\gamma^{IJ}) \quad \text{and} \quad \mathbf{y} \cdot \hat{\hat{\mathbf{W}}}^{IJ} = \mathbf{0}$$

The non-zero second derivatives of $\mathbf{w}_{,\beta}$ then are

$$\mathbf{y} \cdot \widetilde{\widehat{\mathbf{W}}}_{,\beta}^{IJ} = (N_{,\beta}^J \mathbf{y} \cdot \mathbf{L}_\gamma^{JI}) \otimes \mathbf{t}^{\gamma J} \quad (83)$$

$$\mathbf{y} \cdot \widehat{\widehat{\mathbf{W}}}_{,\beta}^{IJ} = \mathbf{t}^{\gamma I} \otimes (N_{,\beta}^I \mathbf{y} \cdot \mathbf{L}_\gamma^{IJ}) \quad (84)$$

The second derivatives of the non-unit director $\mathbf{v} = \mathbf{z} + \mathbf{w}$ with respect to the nodal coordinates and shear vector are given by

$$\widehat{\widehat{\mathbf{V}}}^{IJ} = \widehat{\widehat{\mathbf{Z}}}^{IJ}, \quad \widetilde{\widehat{\mathbf{V}}}^{IJ} = \widetilde{\widehat{\mathbf{W}}}^{IJ}, \quad \widehat{\widetilde{\mathbf{V}}}^{IJ} = \widehat{\widetilde{\mathbf{W}}}^{IJ} \quad \text{and} \quad \widetilde{\widetilde{\mathbf{V}}}^{IJ} = \mathbf{0} \quad (85)$$

The second derivatives of $\mathbf{v}_{,\beta}$ then are

$$\widehat{\widehat{\mathbf{V}}}_{,\beta}^{IJ} = \widehat{\widehat{\mathbf{Z}}}_{,\beta}^{IJ}, \quad \widetilde{\widehat{\mathbf{V}}}_{,\beta}^{IJ} = \widetilde{\widehat{\mathbf{W}}}_{,\beta}^{IJ}, \quad \widehat{\widetilde{\mathbf{V}}}_{,\beta}^{IJ} = \widehat{\widetilde{\mathbf{W}}}_{,\beta}^{IJ} \quad \text{and} \quad \widetilde{\widetilde{\mathbf{V}}}_{,\beta}^{IJ} = \mathbf{0} \quad (86)$$

The last two lines of equations are simply renamed matrices obtained for the non-unit normal \mathbf{z} and the shear vector \mathbf{w} . With these definitions the second derivative of the auxiliary vector $\mathbf{s}_\beta = \mathbf{v}_{,\beta}/|\mathbf{v}|$ with respect to the shear vector is given by

$$\begin{aligned} \mathbf{y} \cdot \widehat{\widehat{\mathbf{S}}}_\beta^{IJ} &= \frac{1}{|\mathbf{v}|} \left[-(\mathbf{y} \cdot \widetilde{\mathbf{S}}_\beta^I) \otimes (\mathbf{d} \cdot \widehat{\mathbf{V}}^J) - (\mathbf{d} \cdot \widetilde{\mathbf{V}}^I) \otimes (\mathbf{y} \cdot \widehat{\mathbf{S}}_\beta^J) \right] \\ &+ \frac{1}{|\mathbf{v}|} \left[\mathbf{y} \cdot \widehat{\widehat{\mathbf{V}}}_{,\beta}^{IJ} - (\mathbf{y} \cdot \mathbf{s}_\beta) (\widetilde{\mathbf{V}}^{I\top} \cdot \widehat{\mathbf{D}}^J + \mathbf{d} \cdot \widehat{\widehat{\mathbf{V}}}^{IJ}) \right] \end{aligned} \quad (87)$$

The other second derivatives of the auxiliary vector, i.e. $\mathbf{y} \cdot \widetilde{\widehat{\mathbf{S}}}_\beta^{IJ}$, $\mathbf{y} \cdot \widehat{\widetilde{\mathbf{S}}}_\beta^{IJ}$ and $\mathbf{y} \cdot \widetilde{\widetilde{\mathbf{S}}}_\beta^{IJ}$, can be determined with (87) by appropriately combining the terms with $\widehat{\widehat{\cdot}}$ and $\widetilde{\widetilde{\cdot}}$ symbols.

Eventually, the second derivatives of unit-length thickness director can be written as

$$\begin{aligned} \mathbf{y} \cdot \widehat{\widehat{\mathbf{D}}}^{IJ} &= \frac{1}{|\mathbf{v}|} \left[-(\mathbf{y} \cdot \widetilde{\mathbf{D}}^I) \otimes (\mathbf{d} \cdot \widehat{\mathbf{V}}^J) - (\mathbf{d} \cdot \widetilde{\mathbf{V}}^I) \otimes (\mathbf{y} \cdot \widehat{\mathbf{D}}^J) \right] \\ &+ \frac{1}{|\mathbf{v}|} \left[\mathbf{y} \cdot \widehat{\widehat{\mathbf{V}}}^{IJ} - (\mathbf{y} \cdot \mathbf{d}) (\widetilde{\mathbf{V}}^{I\top} \cdot \widehat{\mathbf{D}}^J + \mathbf{d} \cdot \widehat{\widehat{\mathbf{V}}}^{IJ}) \right] \end{aligned} \quad (88)$$

and

$$\begin{aligned} \mathbf{y} \cdot \widehat{\widehat{\mathbf{D}}}_{,\beta}^{IJ} &= \mathbf{y} \cdot \widehat{\widehat{\mathbf{S}}}_\beta^{IJ} - (\mathbf{s}_\beta \cdot \widetilde{\mathbf{D}}^I + \mathbf{d} \cdot \widetilde{\mathbf{S}}_\beta^I) \otimes (\mathbf{y} \cdot \widehat{\mathbf{D}}^J) \\ &- (\mathbf{y} \cdot \mathbf{d}) (\widetilde{\mathbf{D}}^{I\top} \cdot \widehat{\mathbf{S}}_\beta^J + \mathbf{s}_\beta \cdot \widehat{\widehat{\mathbf{D}}}^{IJ} + \widetilde{\mathbf{S}}_\beta^{I\top} \cdot \widehat{\mathbf{D}}^J + \mathbf{d} \cdot \widehat{\widehat{\mathbf{S}}}_\beta^{IJ}) \\ &- (\mathbf{y} \cdot \widetilde{\mathbf{D}}^I) \otimes (\mathbf{s}_\beta \cdot \widehat{\mathbf{D}}^J + \mathbf{d} \cdot \widehat{\mathbf{S}}_\beta^J) - (\mathbf{d} \cdot \mathbf{s}_\beta) (\mathbf{y} \cdot \widehat{\widehat{\mathbf{D}}}^{IJ}) \end{aligned} \quad (89)$$

Again, the various combinations of $\widehat{\widehat{\cdot}}$ and $\widetilde{\widetilde{\cdot}}$ in (88) and (89) lead to $\mathbf{y} \cdot \widehat{\widehat{\mathbf{D}}}^{IJ}$, $\mathbf{y} \cdot \widetilde{\widetilde{\mathbf{D}}}^{IJ}$ and $\mathbf{y} \cdot \widetilde{\widehat{\mathbf{D}}}^{IJ}$, as well as, $\mathbf{y} \cdot \widehat{\widehat{\mathbf{D}}}_{,\beta}^{IJ}$, $\mathbf{y} \cdot \widetilde{\widetilde{\mathbf{D}}}_{,\beta}^{IJ}$ and $\mathbf{y} \cdot \widetilde{\widehat{\mathbf{D}}}_{,\beta}^{IJ}$.

REFERENCES

1. K.J. Bathe, F. Brezzi, and S.W. Cho. The MITC7 and MITC9 plate bending elements. *Computers & Structures*, pages 797–814, 1989.
2. T. Belytschko, H. Stolarski, W.K. Liu, N. Carpenter, and J.S.-J. Ong. Stress projection for membrane and shear locking in shell finite elements. *Computer Methods in Applied Mechanics and Engineering*, 51:221–258, 1985.
3. P. Betsch, F. Gruttman, and E. Stein. A 4-node finite shell element for the implementation of general hyperelastic 3d-elasticity at finite strains. *Computer Methods in Applied Mechanics and Engineering*, 130:57–79, 1996.
4. H. Biermann, D. Kristjansson, and D. Zorin. Approximate Boolean operations on free-form solids. In *Proceedings of the 28th annual conference on computer graphics and interactive techniques*, pages 185–194, 2001.
5. M. Bischoff and E. Ramm. Shear deformable shell elements for large strains and rotations. *International Journal for Numerical Methods in Engineering*, 40:4427–4449, 1997.
6. K.U. Bletzinger, M. Bischoff, and E. Ramm. A unified approach for shear-locking-free triangular and rectangular shell finite elements. *Computers & Structures*, 75:321–334, 2000.
7. N. Büchter, E. Ramm, and D. Roehl. Three-dimensional extension of non-linear shell formulation based on the enhanced assumed strain concept. *International Journal for Numerical Methods in Engineering*, 37:2551–2568, 1994.
8. P.G. Ciarlet and V. Lods. Asymptotic analysis of linearly elastic shells. III. Justification of Koiter's shell equations. *Archive for Rational Mechanics and Analysis*, 136:191–200, 1996.

9. F. Cirak and Q. Long. Subdivision shells with exact boundary control and non-manifold geometry. *International Journal for Numerical Methods in Engineering*, DOI: 10.1002/nme.3206, 2011.
10. F. Cirak and M. Ortiz. Fully C^1 -conforming subdivision elements for finite deformation thin-shell analysis. *International Journal for Numerical Methods in Engineering*, 51:813–833, 2001.
11. F. Cirak, M. Ortiz, and P. Schröder. Subdivision surfaces: a new paradigm for thin-shell finite-element analysis. *International Journal for Numerical Methods in Engineering*, 47:2039–2072, 2000.
12. F. Cirak, M.J. Scott, E.K. Antonsson, M. Ortiz, and P. Schröder. Integrated modeling, finite-element analysis, and engineering design for thin-shell structures using subdivision. *Computer-Aided Design*, 34:137–148, 2002.
13. T. DeRose, M. Kass, and T. Truong. Subdivision surfaces in character animation. In *SIGGRAPH 1998 Conference Proceedings*, 1998.
14. E. Grinspun, P. Krysl, and P. Schröder. CHARMS: A simple framework for adaptive simulation. In *SIGGRAPH 2002 Conference Proceedings*, pages 281–290, 2002.
15. F. Gruttmann, E. Stein, and P. Wriggers. Theory and numerics of thin elastic shells with finite rotations. *Archive of Applied Mechanics*, pages 54–67, 1989.
16. C. Loop. Smooth subdivision surfaces based on triangles, master thesis. Master's thesis, Department of Mathematics, University of Utah, 1987.
17. D. Millán, A. Rosolen, and M. Arroyo. Thin shell analysis from scattered points with maximum-entropy approximants. *International Journal for Numerical Methods in Engineering*, Early View, 2010.
18. F.I. Niordson. A note on the strain energy of elastic shells. *International Journal of Solids and Structures*, 7:1573–1579, 1971.
19. E. Oñate and F. Zárate. Extended rotation-free plate and beam elements with shear deformation effects. *International Journal for Numerical Methods in Engineering*, 83:196–227, 2010.
20. D. Peric and D.R.J. Owen. The Morley thin shell finite element for large deformation problems: simplicity versus sophistication. In *Proceedings of the International Conference on Nonlinear Engineering Computations*, pages 121–142, Swansea, 1991.
21. J. Peters and U. Reif. *Subdivision Surfaces*. Springer Series in Geometry and Computing. Springer, 2008.
22. H. Prautzsch, W. Boehm, and M. Paluszny. *Bezier and B-Spline Techniques*. Springer Verlag, 2002.
23. U. Reif. A unified approach to subdivision algorithms near extraordinary vertices. *Computer Aided Geometric Design*, 12:153–174, 1995.
24. C. Sansour. A theory and finite element formulation of shells at finite deformations involving thickness change: Circumventing the use of a rotation tensor. *Archive of Applied Mechanics*, 65:194–216, 1995.
25. C. Sansour. Large strain deformations of elastic shells. Constitutive modelling and finite element analysis. *Computer Methods in Applied Mechanics and Engineering*, 161:1–18, 1998.
26. J.C. Simo, M.S. Rifai, and D.D. Fox. On a stress resultant geometrically exact shell model. Part IV: Variable thickness shells with through-the-thickness stretching. *Computer Methods in Applied Mechanics and Engineering*, 81:91–126, 1990.
27. S. Srinivas and A.K. Rao. Flexure of thick rectangular plates. *Journal of Applied Mechanics - Transactions of the ASME*, pages 298–299, 1973.
28. J. Stam. Evaluation of Loop subdivision surfaces. In *SIGGRAPH 1999 Course Notes*, 1999.
29. G. Strang and G. Fix. *An analysis of the Finite Element Method*. Wellesley-Cambridge Press, Wellesley, 2nd edition, 2008.
30. R.L. Taylor and S. Govindjee. Solution of clamped rectangular plate problems. *Communications in Numerical Methods in Engineering*, 20:757–765, 2004.
31. S.P. Timoshenko and S. Woinowsky-Krieger. *Theory of plates and shells*. McGraw-Hill Book Company, 2nd edition, 1964.
32. J. Warren and H. Weimer. *Subdivision methods for geometric design: A constructive approach*. Morgan Kaufmann, 2001.
33. Z. Xu. A simple and efficient triangular finite element for plate bending. *Acta Mechanica Sinica*, 2:185–192, 1986.
34. D. Zorin and P. Schröder. Subdivision for modeling and animation. *SIGGRAPH 2000 Course Notes*, 2000.